J. Fluid Mech. (2006), *vol.* 565, *pp.* 63–94. © 2006 Cambridge University Press
doi:10.1017/S0022112006001546 Printed in the United Kingdom

Experimental investigation of absolute instability of a rotating-disk boundary layer

By H. OTHMAN AND T. C. CORKE†

Department of Aerospace and Mechanical Engineering, Center for Flow Physics and Control, University of Notre Dame, Notre Dame, IN 46556, USA

(Received 29 June 2005 and in revised form 18 March 2006)

A series of experiments were performed to study the absolute instability of Type I travelling crossflow modes in the boundary layer on a smooth disk rotating at constant speed. The basic flow agreed with analytic theory, and the growth of natural disturbances matched linear theory predictions. Controlled temporal disturbances were introduced by a short-duration air pulse from a hypodermic tube located above the disk and outside the boundary layer. The air pulse was positioned just outboard of the linear-theory critical radius for Type I crossflow modes. A hot-wire sensor primarily sensitive to the azimuthal velocity component, was positioned at different spatial (r, θ) locations on the disk to document the growth of disturbances produced by the air pulses. Ensemble averages conditioned on the air pulses revealed wave packets that evolved in time and space. Two amplitudes of air pulses were used. The lower amplitude was verified to produced wave packets with linear amplitude characteristics. The space–time evolution of the leading and trailing edges of the wave packets were followed past the critical radius for the absolute instability, r_{c_A}. With the lower amplitudes, the spreading of the disturbance wave packets did not continue to grow in time as r_{c_A} was approached. Rather, the spreading of the trailing edge of the wave packet decelerated and asymptotically approached a constant. This result supports previous linear DNS simulations where it was concluded that the absolute instability does not produce a global mode and that linear disturbance wave packets are dominated by the convective instability. The larger-amplitude disturbances were found to produce larger temporal spreading of the wave packets. This was accompanied by a sharp growth in the wave packet amplitude past r_{c_A}. Explanations for this are discussed.

1. Introduction

The boundary-layer flow over a rotating disk in a quiescent fluid has frequently been used as a canonical three-dimensional flow which exemplifies the crossflow instability. In this flow, the instability appears as outward-spiralling waves. These were first detected experimentally in the hot-wire measurements of Smith (1946). The theoretical analysis accompanying experimental results followed later in the classic paper by Gregory, Stuart & Walker (1955).

In theory, the rotating disk flow is attractive because the mean flow has an exact solution. Malik, Wilkinson & Orszag (1981) developed a linear stability analysis of this basic flow that was used to predict the location of transition to turbulence

† Author to whom correspondence should be addressed: tcorke@nd.edu.

https://doi.org/10.1017/S0022112006001546 Published online by Cambridge University Press

by an e^N extrapolation. This produced a satisfactory comparison to the transition locations of previous experiments such as those of Gregory *et al.* (1955), Fedorov *et al.* (1976) and Kobayashi, Kohama & Takamadate (1980), that were based on flow visualization.

Flow visualization of rotating disks tends to emphasize stationary mode development because the modes are fixed with respect to the disk frame of motion. Moreover, stationary modes most often dominate over the theoretically more amplified travelling modes because of their sensitivity to minute surface roughness. For example, Wilkinson & Malik (1985) traced the origin of stationary modes to small randomly placed dust particles on the surface of a 'clean' disk. Corke & Knasiak (1994, 1998) and Corke & Matlis (2004) exploited this by depositing arrays of ink dots on the disk surface to enhance a narrow band of azimuthal and radial wavenumber crossflow modes.

The emphasis of the experiments of Corke & Knasiak and Corke & Matlis was on possible resonant interactions between stationary and travelling Type I crossflow modes. The earlier work used a single hot-wire sensor. The time series were decomposed into separate velocity fluctuations associated with stationary (moving with the disk surface velocity) and travelling modes. Cross-bicoherence analysis of the separate time series revealed a triad phase locking between amplified travelling modes and otherwise linearly damped low azimuthal mode number (of the order of 3 to 5) stationary modes. Subsequent measurements by Corke & Matlis made using a pair of closely spaced sensors, verified wavenumber matching for these modes that confirmed a triad resonance. These results suggested a mechanism for the low azimuthal wavenumber transition front observed in flow visualization on rotating disks such as that of Kobayashi *et al.* (1980).

The analysis by Lingwood (1995) indicated that the rotating disk flow is absolutely unstable. As observational evidence of this, he suggested that values of the transition Reynolds number taken from experimental studies, including those cited above that are primarily based on flow visualization, varied by less than 3 % of the absolute instability critical Reynolds number, $R_{c_A} = 513$ (corrected to be 507 by Lingwood, 1997). The coincidence of the transition Reynolds number is, however, not supported by the results from Wilkinson & Malik (1985) who found in careful low-disturbance experiments using hot-wire evidence to document transition, that $543 \leqslant Re_{tr} \leqslant 556$, placing the average about 8 % higher than R_{c_A}.

Lingwood's (1995) prediction came from a linear stability analysis of the rotating-disk boundary layer that considers the growth of stationary and travelling waves. The viscous analysis assumed a locally parallel flow, streamline curvature and Coriolis effects. It indicated that a critical Reynolds number (or critical radius for a given rotation speed) existed at which disturbances grew temporally, leading to an unbounded linear response and presumably transition. The analytic prediction of the absolute instability critical Reynolds number has subsequently been verified by Pier (2003) and Davies & Carpenter (2003), and is not in dispute. The issue is its role in transition to turbulence of the disk flow.

Lingwood (1996) performed an experimental study designed to capture the temporal growth associated with the absolute instability. This involved introducing unsteady disturbances into the boundary layer and following their development in space and time. The unsteady disturbances were a short duration air pulse that emanated from a hole in the disk surface. The pulse occurred once every disk rotation. The location of the pulse was just outboard of the minimum critical radius for Type I crossflow modes. Lingwood followed the evolution of the azimuthal velocity fluctuations with

https://doi.org/10.1017/S0022112006001546 Published online by Cambridge University Press

a hot-wire sensor placed at different radial and azimuthal distances from the air pulse. Ensemble averages of the time series, correlated with the azimuthal position of the air pulse, revealed wave packets. When the leading and trailing edges of the wave packets were presented in terms of their Reynolds number (radius) and time (azimuthal position with respect to the disk rotation speed) they revealed a tendency for an accelerated advancing of the trailing edge. Unfortunately, Lingwood's measurements stopped short of the critical radius, with the observation that the well-defined structure of the wave packet disintegrated when the critical Reynolds number was approached. The assumption was that this was due to the absolute instability which caused the onset to turbulence.

A different picture has emerged following numerical simulations by Davies & Carpenter (2003). This involved solving the fully linearized Navier–Stokes equations for conditions of the rotating disk flow. In their simulation, they introduced impulse-like disturbances that led to the growth of wave packets. At lower Reynolds numbers, the results were found to reproduce the behavior observed by Lingwood (1996). In particular, there was close agreement to the space–time development of the leading and trailing edges of the wave packets found in the experiment. However, in the absolutely unstable region, the strong temporal growth and upstream propagation was not sustained for long times, and the convective instabilities eventually dominated. Thus they concluded that the absolute instability of the rotating disk boundary layer does not produce a linear amplified global mode, but seemed to be more associated with a transient temporal growth. As such, it could not explain or solely account for the turbulence transition locations observed in experiments.

An answer to this was suggested by Pier (2003) who examined the secondary instability of finite-amplitude waves of the rotating disk flow. The analysis revealed that the primary saturated waves initiated at the critical radius of the absolute instability are already absolutely unstable with respect to secondary perturbations. In this scenario, the primary nonlinear waves are a prerequisite for the development of the secondary instability that leads to transition to turbulence. The primary waves in this case are travelling with respect to the disk frame and have an azimuthal wavenumber (n) of 68 ($\omega_0^{cA} = 50$).

To date, the only experiment we are aware of that was specifically designed to document the absolute instability in the rotating disk flow has been that of Lingwood (1996). Although care was taken in the execution of the experiment, some issues remain. The first is the introduction of the temporal disturbances through a hole in the disk surface. A similar approach was used by Wilkinson *et al.* (1989). Their flow visualization revealed that the hole produced a stationary disturbance wedge that swept outward on a logarithmic arc. Lingwood detected this in hot-wire surveys for the higher disk r.p.m. condition at which most of the results were based, but surmised that the hole produced a disturbance no greater than for unavoidable dust or other surface imperfections. The implication of this is that the background disturbance conditions could have possibly been lower to allow wave packets to be followed closer to R_{c_A}.

A second implication of introducing temporal disturbances through a hole in the disk comes in obtaining an ensemble average of the generated wave packets. The absolute instability applies to travelling modes. To capture these, the ensemble average is conditioned on the time instant of the disturbance pulse. In Lingwood's (1996) experiment, the air pulse occurred when the hole in the disk was directly over a fixed air source. As a result, the disk was always in the same rotation position at the time instant of the disturbance. Therefore the effects of any stationary surface

https://doi.org/10.1017/S0022112006001546 Published online by Cambridge University Press

imperfections (holes, bumps, dust, etc.) producing stationary crossflow modes would also contribute to the ensemble averages.

Finally, in light of the significance that the disturbance amplitudes might have in producing a global instability, it is important to document the wave packet characteristics with regard to linear theory. This should include wall normal amplitude distributions and spatial growth rates.

In light of these issues and the recent simulations and analysis, the objective of our work was to try to improve upon Lingwood's (1996) experiment by:

(i) reducing the background disturbances with particular attention to surface imperfections in order to limit the amplitude of stationary modes and thereby provide the potential for following disturbance wave packets closer to R_{c_A};

(ii) introducing temporal disturbances off the disk surface above the boundary layer, to eliminate the need for stationary disturbance producing holes in the disk surface;

(iii) documenting the basic flow and forced disturbance characteristics to verify linear development so that a direct comparison to Lingwood's (1995) linear analysis and Davies & Carpenter's (2003) linear simulation could be made;

(iv) examining the effect of larger disturbance amplitudes on the development of the wave packets close to R_{c_A}.

The experiment would make use of the same rotating disk facility previously used by Corke & Knasiak (1994, 1998) and Corke & Matlis (2004). This will allow a direct comparison of the basic flow and natural crossflow mode development that had been documented in those previous experiments.

2. Experimental set-up and procedure

2.1. *Set-up*

The rotating disk facility consists of a polished aluminium disk mounted on an air-bearing with an integrated d.c.-motor. The d.c.-motor is controlled by a dedicated digital controller which takes feedback from an optical encoder mounted on the shaft of the motor. The whole system leads to minimum vibration of the disk and a constant rotation speed to within 0.003 %. The measurement surface consisted of a 2.54 cm thick, 45.72 cm diameter aluminium disk. The disk was ground and diamond lapped to be flat and parallel to 0.0038 mm. The surface of the disk was polished to a 2 μm finish. A photograph of the rotating disk set-up is shown in figure 1(*a*).

A motorized traversing mechanism was mounted above the surface of the disk. It allowed two directions of motion: radial and wall-normal, with an accuracy of 0.025 mm, and 0.00025 mm, respectively. The motion in both directions was controlled by stepper motors. A Linear Variable Differential Transducer (LVDT) motion sensor provided feedback for the wall-normal motion. The traversing mechanism was controlled through software by a digital data acquisition and control (DAC) computer.

Special care was taken to position the hot-wire sensor accurately above the surface of the disk. For this we used a cathetometer which was a magnifying telescope with a graticule. This was mounted on a slider that was translated in the vertical direction with a micrometer. The total resolution of the system was 0.002 mm. The absolute distance of the sensor from the disk was determined by taking half the distance between the sensor and its reflection off the surface.

To obtain velocity measurements, a constant-temperature hot-wire anemometer was used. The hot-wire probe was mounted in the traversing mechanism and positioned

https://doi.org/10.1017/S0022112006001546 Published online by Cambridge University Press

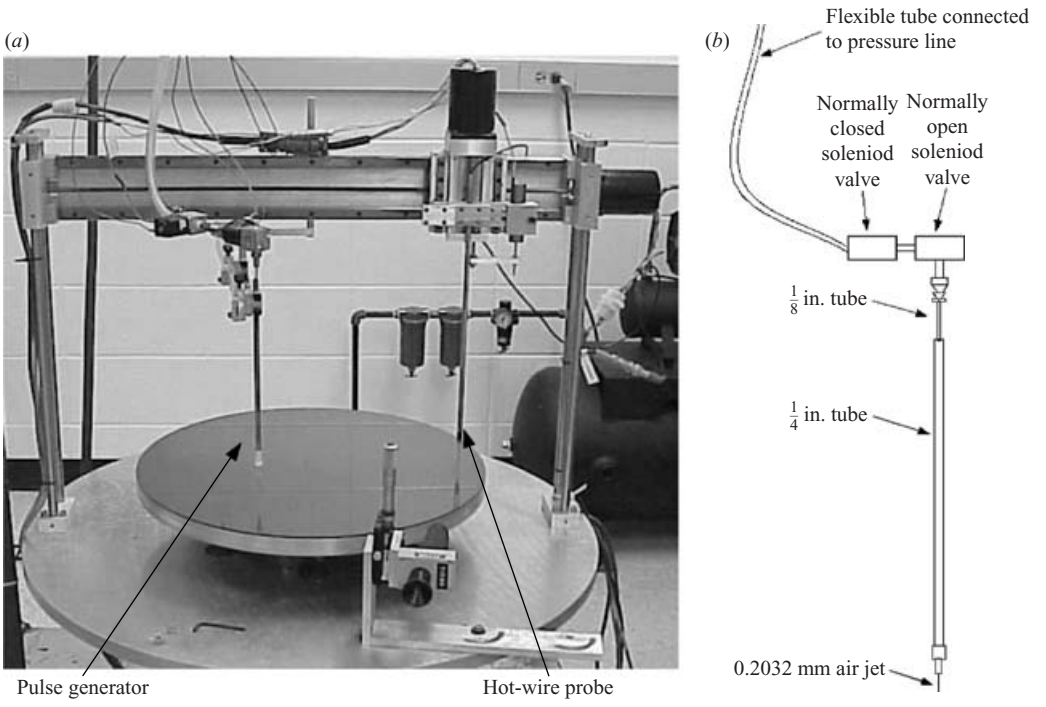


FIGURE 1. (*a*) The rotating disk set-up and (*b*) schematic of air pulse generator used to introduce temporal disturbances in the boundary layer.

under computer control. The sensor was oriented so that it would primarily sense the azimuthal velocity component, U_θ.

The hot-wire sensor was calibrated in a separate calibration jet facility with a known reference velocity. A fourth-order polynomial was used to fit the velocity-voltage data pairs. This polynomial was then used to convert voltages to velocities measured in the disk flow. The accuracy of the calibration was 0.09 % of the maximum disk surface velocity.

The anemometer output was divided into a.c. and d.c. signals. The a.c. signal was obtained by passing the analogue signal through a band-pass filter with the high-pass frequency cutoff set to remove the d.c. ($\geqslant$0.1 Hz), and the low-pass frequency cutoff set at half the sampling frequency to prevent frequency aliasing. The filtered a.c. signal was amplified to use the full range of the analogue-to-digital (A/D) converter and thereby minimize digital quantization error. The d.c. containing signal was separately d.c.-shifted and amplified. Following this analogue conditioning, the a.c. and d.c. signals were input to the A/D converter in the data acquisition computer.

2.2. *Air-pulse disturbance generator*

The disturbance generator consisted of a custom-designed micro air jet that was suspended above the disk outside of the boundary layer. The air in the jet exited from a hypodermic tube with a 0.203 mm inside diameter. The tube was part of an assembly that allowed it to be held rigidly from a mount on the traversing system cross-member. The air pulse generator is shown in the set-up in figure 1(*a*). A schematic drawing of the assembly is shown in figure 1(*b*). The assembly was supplied with a pressure regulated air source. Two air solenoid valves, one normally closed and the other

https://doi.org/10.1017/S0022112006001546 Published online by Cambridge University Press

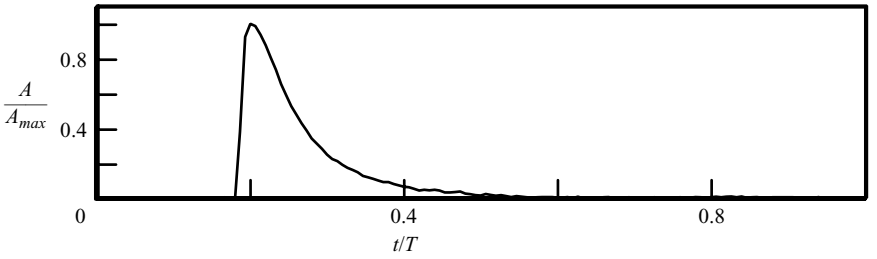


FIGURE 2. Ensemble average of the velocity pulse produced by the air pulse generator that was measured 1 cm from air pulse jet exit.

Input conditions	
Disk r.p.m.	1000
ω	$104.7\,\mathrm{s}^{-1}$
r_{c_I}	11.1 cm
$Re_{c_I} = r_{c_I}\left(\frac{\omega}{\nu}\right)^{1/2}$	285 (theory)
Re_{c_A}	507.3 (Lingwood 1997)
r_{c_A}	19.75 cm
r_{pulse}	12.1 cm
Re_{pulse}	311

TABLE 1. Experimental conditions.

normally open, were used to generate a short duration air pulse. A single solenoid valve (normally closed) did not close sufficiently fast to achieve the desired duration of the pulse. The use of the second (normally open) valve provided a positive control to end the air pulse. The valves were operated from voltage time series provided by the data acquisition computer. Figure 2 shows the average velocity time series for a large ensemble of air pulses measured by a hot-wire sensor placed approximately 1 cm from the tube exit. The time axis is normalized by the time for one rotation of the disk, T, for the conditions of the experiment. The maximum time extent of the pulse is approximately 20 % of the disk rotation. This was found to be sufficiently short to produce isolated wave packets and follow their evolution.

The air pulser assembly could be moved in the wall-normal direction which allowed a degree of adjustment to control the spatial extent and strength of the air pulse. The strength was also controllable through the air-supply pressure. For all measurements, the distance of the air pulse jet from the disk surface was 4 mm. Based on mean velocity profiles, the boundary-layer thickness was approximately 2 mm.

The air pulse assembly could also be located at different radial and azimuthal locations, so we could achieve the relative separations between the hot-wire and pulse generator required to map out the space–time evolution of the generated wave packets. For the results reported here, the radial position of the pulse generator was kept fixed at $r = 12.1$ cm, which corresponded to $R = 311$ used by Lingwood (1996).

2.3. *Experimental conditions*

The disk was operated at the conditions used by Corke & Knasiak (1994, 1998) and Corke & Matlis (2004). The experimental conditions are summarized in table 1.

https://doi.org/10.1017/S0022112006001546 Published online by Cambridge University Press

r (cm)	r/r_{c_I}	r/r_{c_A}	Re	r (cm)	r/r_{c_I}	r/r_{c_A}	Re
7.00	0.6306	0.3548	180	18.00	1.6216	0.9107	462†
8.00	0.7207	0.4041	205	18.50	1.6667	0.9363	475
9.00	0.8108	0.4553	231	19.00	1.7117	0.9620	488†
10.00	0.9009	0.5066	257	19.50	1.7568	0.9876	501
11.00	0.9910	0.5559	282	19.75	1.7793	0.9994	507
12.00	1.0811	0.6071	308†	20.00	1.8018	1.0112	513†
13.00	1.1712	0.6584	334†	20.25	1.8243	1.0250	520
14.00	1.2613	0.7077	359†	20.50	1.8468	1.0369	526
15.00	1.3514	0.7589	385†	21.00	1.8919	1.0625	539†
16.00	1.4414	0.8101	411†	21.50	1.9369	1.0881	552
17.00	1.5315	0.8614	437†	22.00	1.9820	1.1137	565†
				22.50	2.0270	1.1392	578†

† Measurement locations with disturbance pulse.

TABLE 2. Measurement radial locations.

Based on these, the locations of the critical radii for the Type I crossflow mode linear growth, r_{c_I} and absolute instability, r_{c_A}, were defined.

The velocity was measured at 22 radial positions that bracketed the two critical radii. These are summarized in table 2. Wall normal points were progressively spaced in the wall-normal direction, approximately according to the mean velocity gradient. Closest to the disk surface, the points are 0.0381 mm apart; furthest from the disk surface, the points are 0.286 mm apart. The total traverse encompassed 3.962 mm. This was the same for all the radial locations.

Our observations as well as those in the literature (Wilkinson & Malik 1985; Corke & Knasiak 1998; Saric, Reed & White 2003) emphasize the extreme sensitivity of Type 1 crossflow modes to surface imperfections such as μm-sized dust particles. Therefore special care was taken to keep the disk surface clean by wiping the surface before each data set. With this approach, we (Othman 2005) verified excellent repeatability of R_{tr} over the course of the experiment.

2.4. *Experimental approach and time-series analysis*

Two types of measurement were performed: those that documented the basic flow and its linear stability characteristics, and those that documented the evolution of wave packets produced by the air pulse disturbances. Documentation of the basic flow involved measurement of wall normal profiles of velocity time series at different radial locations (table 2). These consisted of statistically independent records of contiguous voltage series proportional to the azimuthal velocity (U_θ) taken at 24 discrete points in the wall-normal (z) direction. The contiguous records were 1024 points in length which corresponded to 6.82 revolutions of the disk at the sampling frequency of 2500 samples s^{-1}. Given the disk rotation frequency and sampling frequency, there were 150 sample points per disk revolution. In spectral analysis of the time series, this allowed us to resolve stationary (moving with the disk rotation velocity) modes with azimuthal mode numbers (n) of up to 75. The absolute instability corresponds to travelling modes. The dimensionless frequency of these is in the range of ω_0^{cA} from 50 to 60 (Pier 2003), giving real frequencies from 833 to 1000 Hz. These were fully resolved by the sampling frequency used.

https://doi.org/10.1017/S0022112006001546 Published online by Cambridge University Press

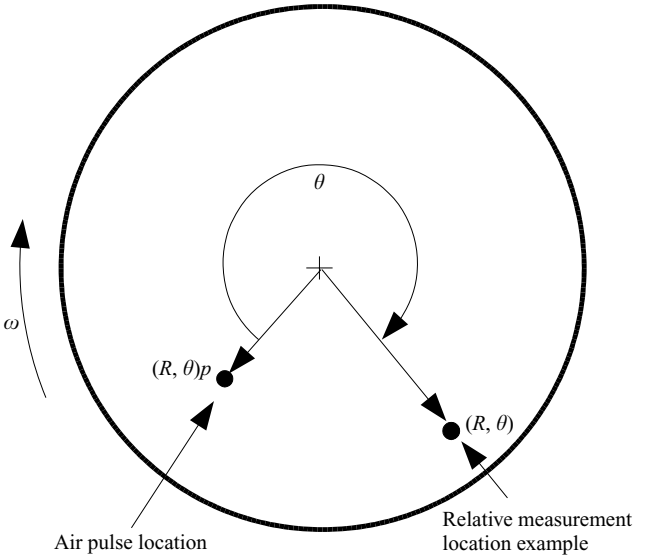


FIGURE 3. Schematic defining the relative positions of the air pulse generator and hot-wire sensor used in documenting the space–time development of disturbance wave packets. Radius Reynolds number of the pulse generator was fixed at $Re = 311$ which was the same as Lingwood (1996).

	Angle (deg.)		Angle (deg.)
1	10	8	190
2	20	9	220
3	40	10	250
4	70	11	280
5	100	12	310
6	130	13	340
7	160	14	350

TABLE 3. Relative angles between the hot wire and the air pulser.

The same sampling rate was used in documenting the evolution of wave packets produced by the air pulse generator. However, the velocity time series acquisition was coordinated with the pulse initiation. The approach was to start the acquisition of the hot-wire sensor voltage a short time before triggering the air pulse. The voltage signal used to initiate the air pulse was also simultaneously sampled with the hot-wire time series so that it could be used as a time reference for ensemble averaging. Typically, 1000 records were used to form the ensemble average. There was no correlation between the time-series acquisition and the disk rotational position. Therefore, the ensemble average yielded only features that were related to the disturbance pulse, and travelling with respect to the disk rotation frame of reference.

The relative positions of the air pulse generator and hot-wire sensor varied. A schematic representation is shown in figure 3. In all cases, the radial location of the pulse generator was fixed at 12.1 cm ($R = 311$). However, its azimuthal position was varied to produce different azimuthal spacings, θ, between the pulse generator and the hot wire. Table 3 gives the relative angles used in the experiment. At each of

https://doi.org/10.1017/S0022112006001546 Published online by Cambridge University Press

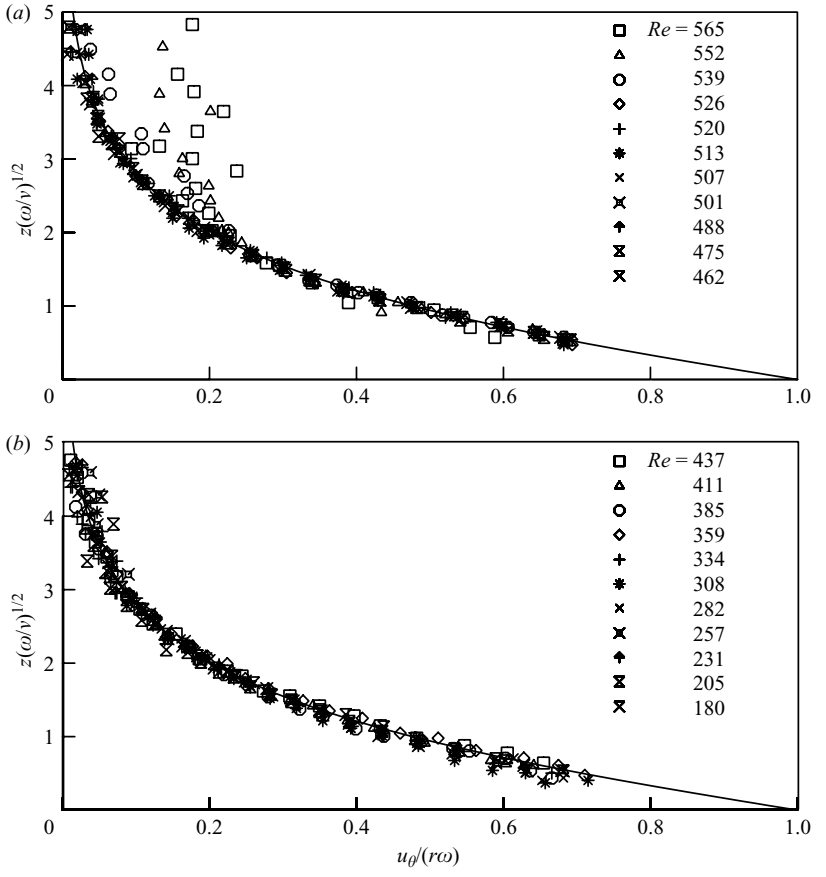


FIGURE 4. Mean profiles of azimuthal velocity component at different radial Reynolds numbers. Solid curve, theoretical profile for an infinite radius disk.

these, velocity time series were recorded at all of the radial positions indicated by the footnote in table 2.

In all cases, the hot-wire voltages were converted to velocities using a fourth-order polynomial calibration equation. The polynomial coefficients were determined during calibration runs by a least-squares fit against known velocity points. Spectral analysis was performed using discrete fast Fourier transforms (FFT). The typical FFT size was 128 points. This gave a frequency resolution of 19.5 Hz, or for stationary modes $\Delta n \simeq 1$. Amplitudes corresponding to spectral peaks were converted to r.m.s. by taking the areas under the peaks and normalizing them by the frequency bandwidth. These were used to determine the spatial amplitude distributions for particular modes.

3. Results

3.1. *Basic flow and natural instability development*

Although our principle objective was to study the absolute instability of the rotating disk boundary layer, it was important to verify that the basic flow and its linear stability characteristics agreed with theory. The basic flow is represented in the mean velocity profiles shown in figure 4. For these, the wall coordinate and azimuthal velocity are presented in similarity form, $z\sqrt{\omega/\nu}$, and $u_\theta/(r\omega)$, respectively.

https://doi.org/10.1017/S0022112006001546 Published online by Cambridge University Press

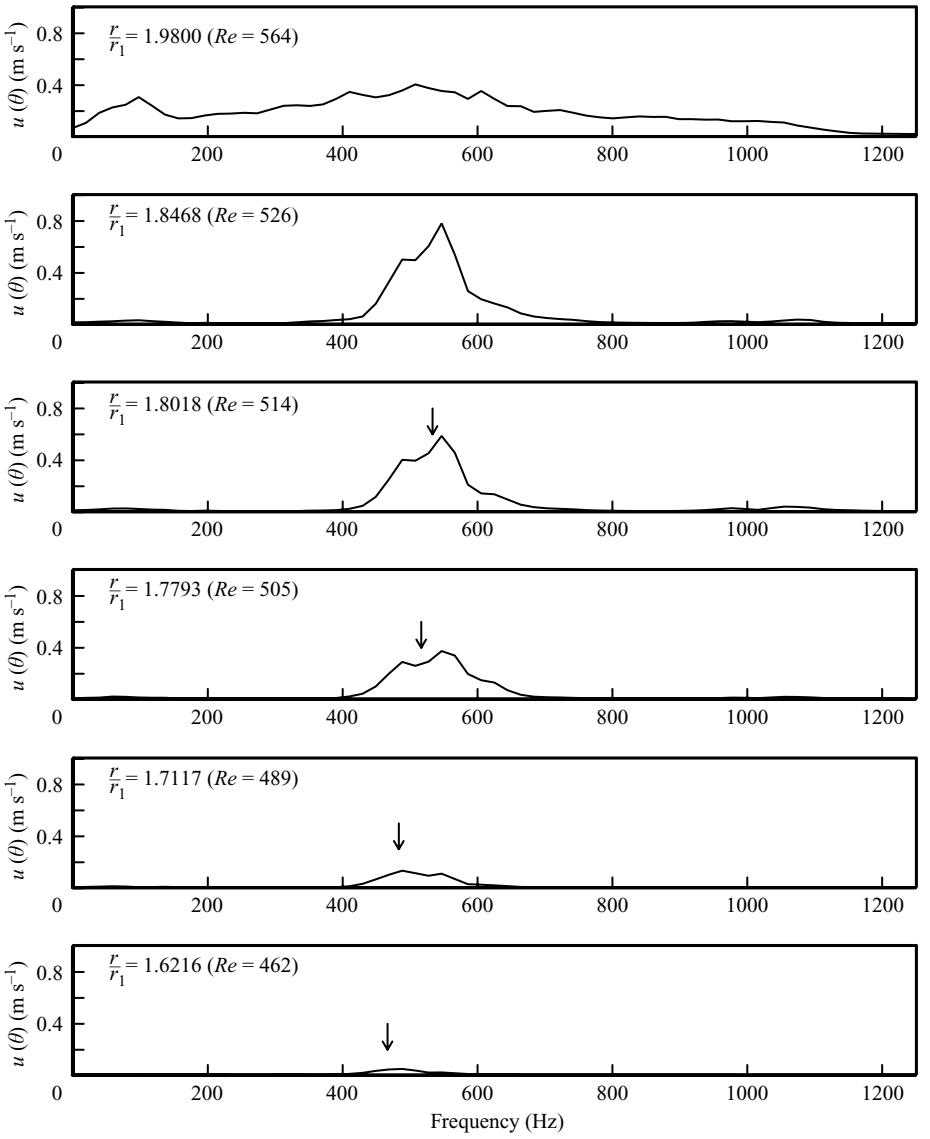


FIGURE 5. Spectra of azimuthal velocity fluctuations at different radial positions (Reynolds numbers) of the basic flow on the disk.

The different symbols represent Reynolds numbers (radii) where the profiles were measured. The solid curve is the theoretical (laminar) mean velocity profile for an infinite radius rotating disk. At the lower radii, the measured velocity profiles show excellent agreement with the theoretical profile. The deviation of the mean velocity profiles from the laminar distribution at larger radii is an indication of the mean flow distortion caused by the growth of crossflow modes to nonlinear amplitudes. For the conditions on the disk this occurred at $R \simeq 539$. Note that this agrees well with the transition Reynolds number found on a 'clean' disk by Wilkinson & Malik (1985), and is well beyond the absolute instability critical Reynolds number (507.3).

The linear stability of the basic flow is first documented through the spectra of azimuthal velocity fluctuations at different radial locations on the disk (figure 5).

https://doi.org/10.1017/S0022112006001546 Published online by Cambridge University Press

These were taken at the height above the surface where the fluctuation amplitude is a maximum ($z\sqrt{\omega/\nu} \simeq 1.5$). The velocity fluctuations are presumed to represent combinations of stationary and travelling Types 1 and 2 crossflow modes. Although the Type 2 mode has a lower critical Reynolds number of 69 (Faller 1991), its amplification rate is considerably smaller than the Type 1 mode. In addition, the Type 2 instabilities seem to appear in proportion to the amount and amplitude of external disturbances (Faller 1991). Therefore, experiments with carefully controlled disturbance conditions, are expected to be largely dominated by Type 1 modes.

We have made no attempt to decompose the velocity fluctuations into the contributions due to stationary and travelling Type 1 modes (such as Corke & Knasiak 1998). Therefore, the abscissa of the spectral plots is shown as frequency, and not normalized by the disk frequency to represent the stationary azimuthal mode number, n. Linear theory and confirming measurements by Corke & Matlis (2004) indicate that the most amplified travelling modes move at approximately 85 % of the local disk surface velocity.

At any supercritical radii ($r/r_{c_I} > 1$), we expect to see a range of frequencies (mode numbers) that represent the progression of growing and decaying crossflow waves. For stationary modes, $n = \beta R$ (see Malik, Wilkinson & Orszag 1981), where β is the azimuthal wavenumber. The most amplified β is 0.0698 so that $n \propto R$, or the most amplified frequency varies linearly with radius. This result leads to the commonly observed spiral angle of stationary crossflow modes of $\psi = 11.1^\circ$ (Corke & Knasiak 1998).

The velocity spectra shown in figure 5 correspond to progressively increasing Reynolds numbers (radii) from 462 to 564. Starting at the lowest Reynolds number in the figure, there appears a relatively narrow band of frequencies in which the amplitude is smoothly above the lower background level. This band is observed to grow in amplitude and progressively shift towards higher frequencies as the radius (Reynolds number) increases. The arrows above each curve indicate the frequency based on $n = \beta R$. Throughout the Reynolds range up to 514, the arrows correspond reasonably well with the largest amplitudes in the spectra.

This trend in the growth and shift of the dominant frequencies continues at least until $R = 526$ in figure 5. We note that this is beyond R_{c_A}. At further radii corresponding to $R = 564$, the spectrum is broadband, signifying a transition to turbulent flow. This also corresponds with a large mean flow distortion that was exhibited in the mean velocity profile at this location in figure 4.

The amplitude distribution in the wall-normal direction for the most amplified frequency corresponding to the arrow above the spectra at $R = 462$ is shown in figure 6. Also included are the distributions at Reynolds numbers that bracket R_{c_A}. The curve corresponds to the linear theory eigenfunction based on $\beta = 0.0698$ and the most amplified $\alpha_r = 0.354$. The measured amplitude distributions agree fairly well with the linear eigenfunction indicating that velocity fluctuations are associated with the linear Type 1 crossflow mode.

Another check of the stability of the basic flow comes in examining the spatial amplification rates. This is presented in figure 7 for four selected frequencies. The lowest frequency corresponds to that for the wall-normal distributions in figure 6. The others are progressively higher, with 566 Hz being the approximate most amplified just upstream of R_{c_A}. The r.m.s. amplitudes of these, $u'(\theta)$, have been normalized by R_{c_I} to express the amplification rate. These are shown on a log scale to emphasize exponential growth.

https://doi.org/10.1017/S0022112006001546 Published online by Cambridge University Press

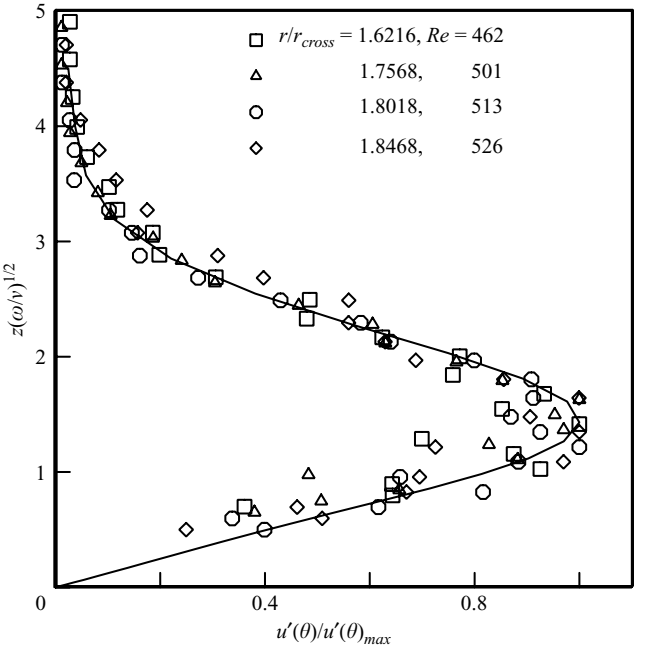


FIGURE 6. Wall-normal amplitude distribution at different radial location Reynolds numbers of the basic flow for the frequency ($f = 466$ Hz) corresponding to the arrow above spectra at $Re = 462$ in figure 5. Curve corresponds to linear-theory eigenfunction for $\beta = 0.0698$ and $\alpha_r = 0.354$.

For all the frequencies shown in figure 7, there is a clear linear (exponential) growth region. The respective straight lines resulted from a least-squares curve fit of the data to an exponential function. The slopes of these lines are the respective amplification rates. These have been summarized in table 4. The amplification rates are very close to those found by Corke & Knasiak (1998) using wall 'dots' to enhance specific azimuthal mode numbers, and a method to separate the velocity fluctuations into those associated with stationary or travelling modes. For $n = 27$ and $f = 450$ Hz they obtained $-\alpha_i/Re_{c_l} = 0.034$ and 0.041, respectively. For a travelling mode at 483 Hz, they found $-\alpha_i/Re_{c_l} = 0.049$. Mack (1985) obtained a value of $-\alpha_i/Re_{c_l} = 0.039$ at a Reynolds number of 400 for an envelope of growing waves that had been excited by a single isolated roughness element, and a largest growth value of 0.043 for pure waves. Spalart (1991) also found a value of 0.045 for random stationary disturbances at $R = 440$.

The content of the time series used in obtaining the spectra for isolating the growth rates at specific frequencies contain contributions from both stationary and travelling modes. In theory, their growth rates are different, with the travelling modes being slightly more amplified. Therefore within this uncertainty, the amplification rates measured here are in reasonable agreement with theoretical predictions.

The results in figure 7 are not intended, or capable, of determining the critical Reynolds numbers for the respective frequencies because the digitally acquired hot-wire sensor cannot measure asymptotically small fluctuations. The lower measurement limit of fluctuation amplitudes in our case is specified by the r.m.s. quantization noise. Accounting for this, and putting it in terms of a minimum r.m.s. velocity fluctuation based on $\mathrm{d}E/\mathrm{d}U$ from the hot-wire calibration for U at u'_{max} in the disk

https://doi.org/10.1017/S0022112006001546 Published online by Cambridge University Press

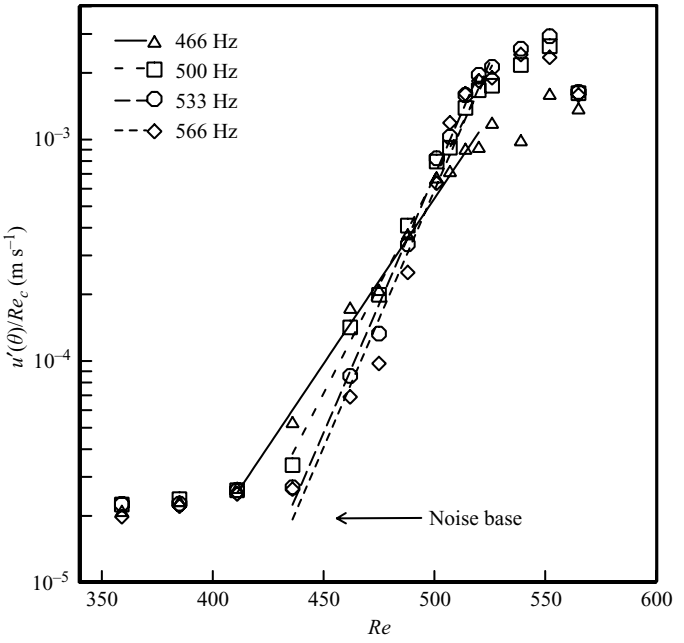


FIGURE 7. Radial growth in amplitude of different frequencies that are in the most amplified band for the basic flow. Lines correspond to a least-square curve fit of the data to an exponential function. The slopes of the lines corresponding to the amplification rates are given in Table 4.

f (Hz)	$-\alpha_i/Re_{c_l}$
466	0.034
500	0.044
513	0.053
566	0.055

TABLE 4. Amplification rates based on figure 7.

boundary layer, the quantization noise corresponds approximately to 0.0057 m s^{-1}, or $u'/U_{max} = 0.00049$ based on U_{max} at r_{c_l}. The arrow shown in figure 7 signifies this noise base. As indicated in our objectives, we took great care to minimize disturbances. As a result, the growing modes start at low initial amplitudes that cannot be detected until they exceed our noise base limit. The actual approach to determine R_c is to introduce larger-amplitude disturbances with known wavenumber content at subcritical Reynolds numbers and then measure the spatial amplitude development to determine the location of neutral growth. This was not our intention.

The location of the amplitude saturation and decay is another indication of where transition to turbulence is occurring. In figure 7, this occurs at approximately $R \simeq 540$, which also corresponds to where the mean flow profiles began to deviate from the theoretical laminar profile. Thus, both measurements indicate natural transition to turbulence to be occurring past R_{c_A}.

https://doi.org/10.1017/S0022112006001546 Published online by Cambridge University Press

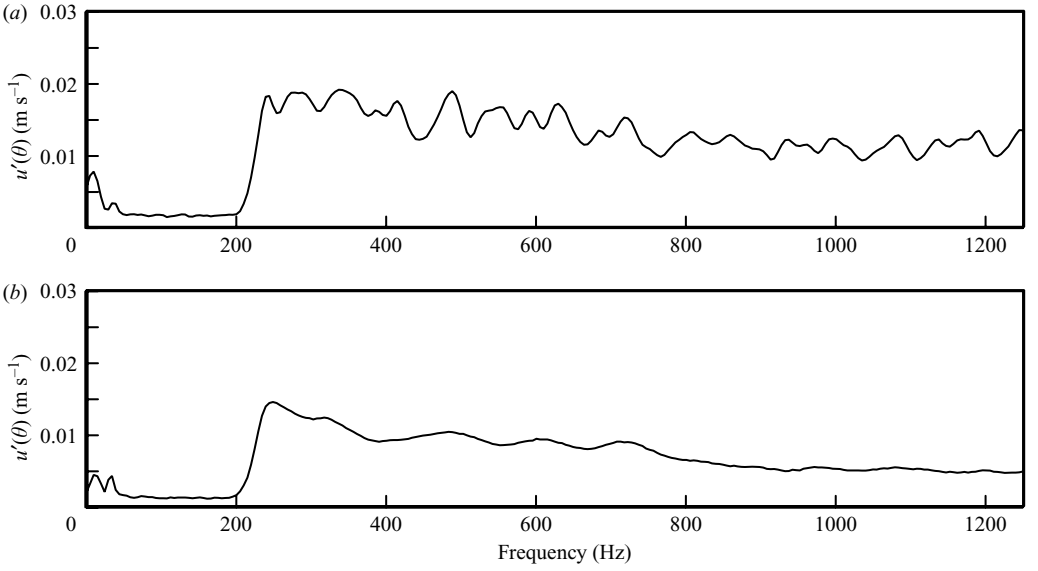


FIGURE 8. Spectra of azimuthal velocity fluctuations in boundary layer produced by air pulse at two amplitude conditions used in experiments. (*a*) 80 p.s.i.g. (*b*) 28 p.s.i.g. Measurements were made at $R = 347$ and $\theta = 20°$.

3.2. *Temporal mode development*

Short-duration air-pulse disturbances were introduced at a fixed radius in order to follow the development of wave packets and discern their amplitude growth in space and time. The radial location of the disturbance source corresponded to $R = 311$ ($r/r_{c_l} = 1.0900$), which was the same as that of Lingwood (1996). After some initial experiments, two pressure amplitudes were selected. These are denoted by the laboratory pressure settings, 28 and 80 p.s.i.g. The lower pressure amplitude was verified to give linear development to beyond the absolute instability radius. As expressed in the objectives, this was important in order to compare directly to the linear analysis of Lingwood (1995) and the linear simulation of Davies & Carpenter (2003). The use of the higher pressure was intended to examine the effect of larger disturbance amplitudes on the development of the wave packets close to R_{c_A}, with the possibility of producing the nonlinear scenario shown by Pier (2003) to produce a global instability.

Spectra of azimuthal velocity fluctuations in the boundary layer produced by the air pulse at the two amplitude conditions are shown in figure 8. These were measured at a close radius and angle to the pulser, corresponding to $R = 347$ and $\theta = 20°$. The sensor height from the wall corresponds to the location of $u'(\theta)_{max}$.

At this close distance to the air pulse, the disturbance feeds a broad range of frequencies that will eventually be selectively amplified by the flow. The spectra reveal that both pulse amplitude conditions put energy into a range of frequencies that are capable of being amplified by the Type I crossflow modes ($f \geqslant 300$ Hz), and being a part of the absolute instability ($f \geqslant 833$ Hz). The higher pulse amplitude produces higher fluctuation levels, with about the same frequency distribution as the lower amplitude pulse. This is discussed in the next section.

https://doi.org/10.1017/S0022112006001546 Published online by Cambridge University Press

3.2.1. *Low-amplitude pulse*

The intention of the lower amplitude air pulse was to produce disturbance wave packets with linear characteristics. One check on the linear character of the disturbances can come by comparing their wall-normal amplitude distributions to the the linear theory eigenfunction. This is done in figures 9 and 10.

Figure 9 shows ensemble-averaged azimuthal velocity, $u(\theta)$, time series measured at different heights above the wall at $R = 437$ and $\theta = 220°$. The ensemble averaging reveals clear wave packets. The velocity time series are shown as a dashed curve. These have a periodic appearance with an amplitude that varies to define the leading and trailing edges of the packet. The amplitude envelope of the velocity fluctuations is shown as a solid curve. This was determined using a digital Hilbert transform of the digitally band-passed ensemble time series for $450 \leqslant f \leqslant 1250$ Hz. Note that these frequencies encompass the most amplified linear modes as well as the absolutely unstable modes. Details of this are contained in Othman (2005).

The maximum envelope amplitude of the wave packets at the different heights in figure 9 are compared to the linear theory eigenfunction in figure 10. The eigenfunction, shown as the solid curve, is the one used in figure 6 and corresponds to $R = 462$. Also shown in figure 10 is the amplitude distribution for another set of wave packets measured at $R = 513$ and $\theta = 280°$. This location is just past R_{c_A}.

Both of the wave packet amplitude distributions agree well with the linear eigenfunction. This supports that premise that the velocity fluctuations in the wave packets are primarily associated with Type I crossflow modes, and that their amplitudes satisfy linear theory assumptions.

Another indication of the linear character of the disturbance wave packets comes from examining their spatial amplitude growth. With temporal disturbances emanating at a point, this is not as straightforward as for the natural developing modes. For example, figure 11 shows velocity spectra at different azimuthal locations for one radial position ($R = 437$). These spectra correspond to the z height of the amplitude maximum. They demonstrated the evolution of the band of frequencies of velocity fluctuations in the disturbance wave packet as it evolves from the source.

In order to show the full evolution of the disturbances in space, spectra like those in figure 11 but at all of the measured radii, were compiled to produce figure 12. Figure 12(a) shows the amplitudes in (r, θ)-space at a frequency of 533 and figure 12(b) at 1000 Hz, where the former is near the most amplified (see figure 7) and the latter is in the band of predicted absolute instability ($f \geqslant 833$ Hz). The amplitudes have been normalized by their minimum value and presented as log-level contours to highlight exponential growth. The solid curve corresponds to a log-spiral with a spiral angle of $\psi = 11.1°$ that is based on $\beta = 0.0698$ and the most amplified $\alpha_r = 0.354$. Our expectation is that the disturbances from the pressure pulse source will travel outward along the log-spiral trajectory. Based on the amplitude contours, this expectation appears reasonable.

In order to determine whether the two discrete frequencies in the disturbance wave packet are growing linearly, amplitudes along the log-spiral in figures 12(a) and 12(b) were compiled and plotted in figure 13. This shows the actual $u'(\theta)$ values normalized by R_{c_I} as in figure 7. The solid line corresponds to an exponential fit to the values, and the exponent of the fit corresponding to $-\alpha_i / R_{c_I}$ is given in the figure. Also shown by the dashed line is the location of R_{c_A}.

There are two points to be made from figure 13. The first is that both of the frequencies exhibit linear growth at least up to R_{c_A}. This was an important issue in our objectives in order to satisfy linear theory initial conditions used in the absolute

https://doi.org/10.1017/S0022112006001546 Published online by Cambridge University Press

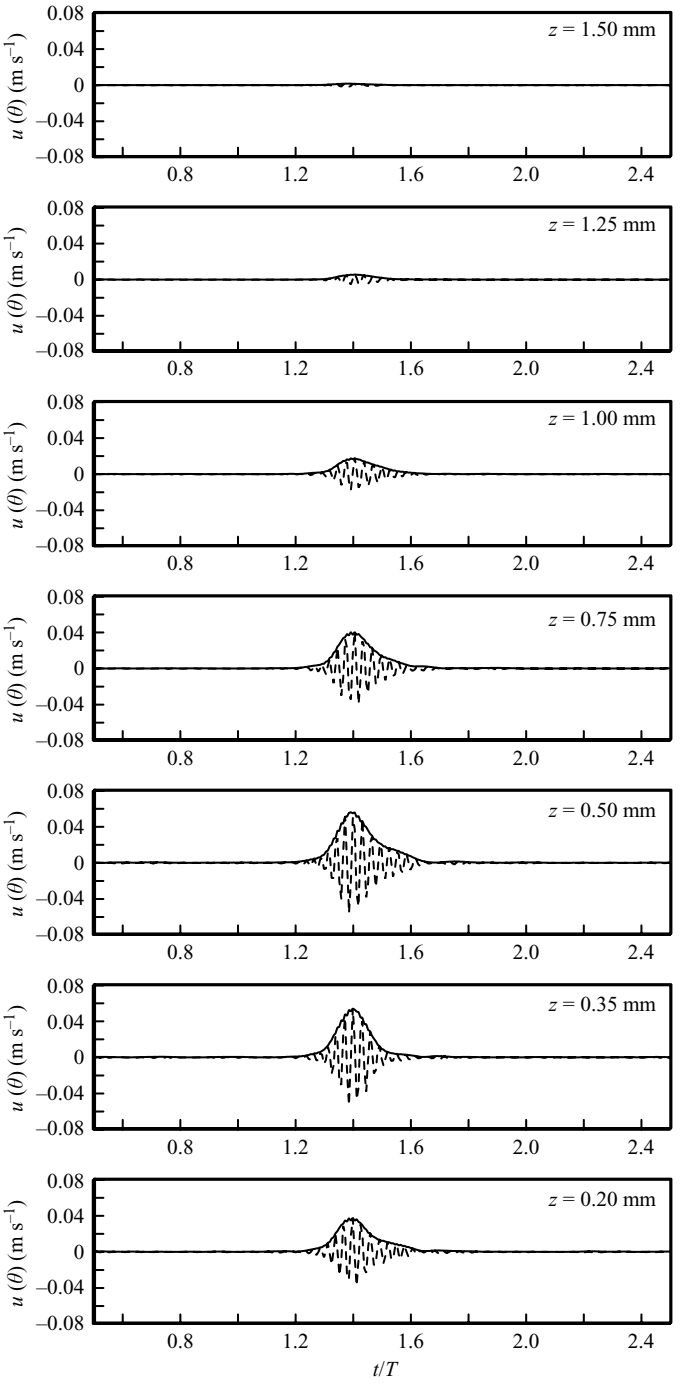


FIGURE 9. Ensemble-averaged azimuthal velocity time series measured at different heights above disk surface for lower (28 p.s.i.) amplitude pulse. $r = 17.0\,\mathrm{cm}$; $\theta = 220°$. Measurements are at $Re = 437$. Dashed curve, ensemble-averaged velocity; solid curve, amplitude envelope produced by a digital Hilbert filter of our design.

https://doi.org/10.1017/S0022112006001546 Published online by Cambridge University Press

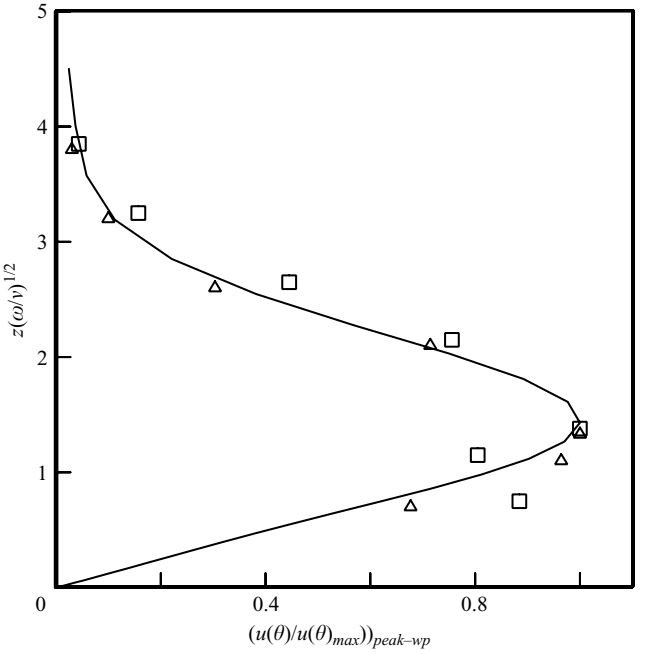


FIGURE 10. Wall normal distribution of the maximum wave packet envelope amplitude at $Re = 437$ and 513 for lower (28 p.s.i.) amplitude pulse. The curve is the linear theory eigenfunction at $Re = 462$ shown in figure 6. Δ, $Re = 437$, $\theta = 220°$; $\square$, $Re = 513$, $\theta = 280°$.

instability analysis. Note, that we expect the amplification rates measured along the log spiral to be lower than those in figure 7, which were measured in the radial direction. The second point from this figure is that even at the lower disturbance amplitudes produced by the lower pressure (28 psi) pulse, there is growth in energy over the whole frequency range of importance.

The evolution of wave packets was documented by ensemble-averaged velocity measurements at different radial and azimuthal distances (table 2) from the air-pulse disturbance generator. A sample of these is shown in figure 14. These are at $R = 514$, which is just supercritical for absolute instability growth based on Lingwood (1996). The different plots correspond to increasing azimuthal angles from the disturbance generator. The time taken for the wave packets to reach the velocity sensor increases with the azimuthal spacing. Here, time has been normalized by the disk rotation time T. For time increasing from left to right, the leading edges of the wave packets are on the left-hand side, and the trailing edges are on the right. Note that at this radius for the sensor angle locations, the wave packet has traveled from one to two times around the disk.

Of particular interest with the absolute instability mechanism is the spreading of the wave packets in time. This has been measured by analysing the evolution of wave packets at all of the locations given in table 2 in which leading and trailing edges were identifiable. Where these were identifiable, the process for determining the edges of the wave packet was to use the amplitude envelope calculated from the Hilbert transform, locate the peak in the envelope amplitude, then move forward and backwards in time to find the point where the amplitude envelope reached the

https://doi.org/10.1017/S0022112006001546 Published online by Cambridge University Press

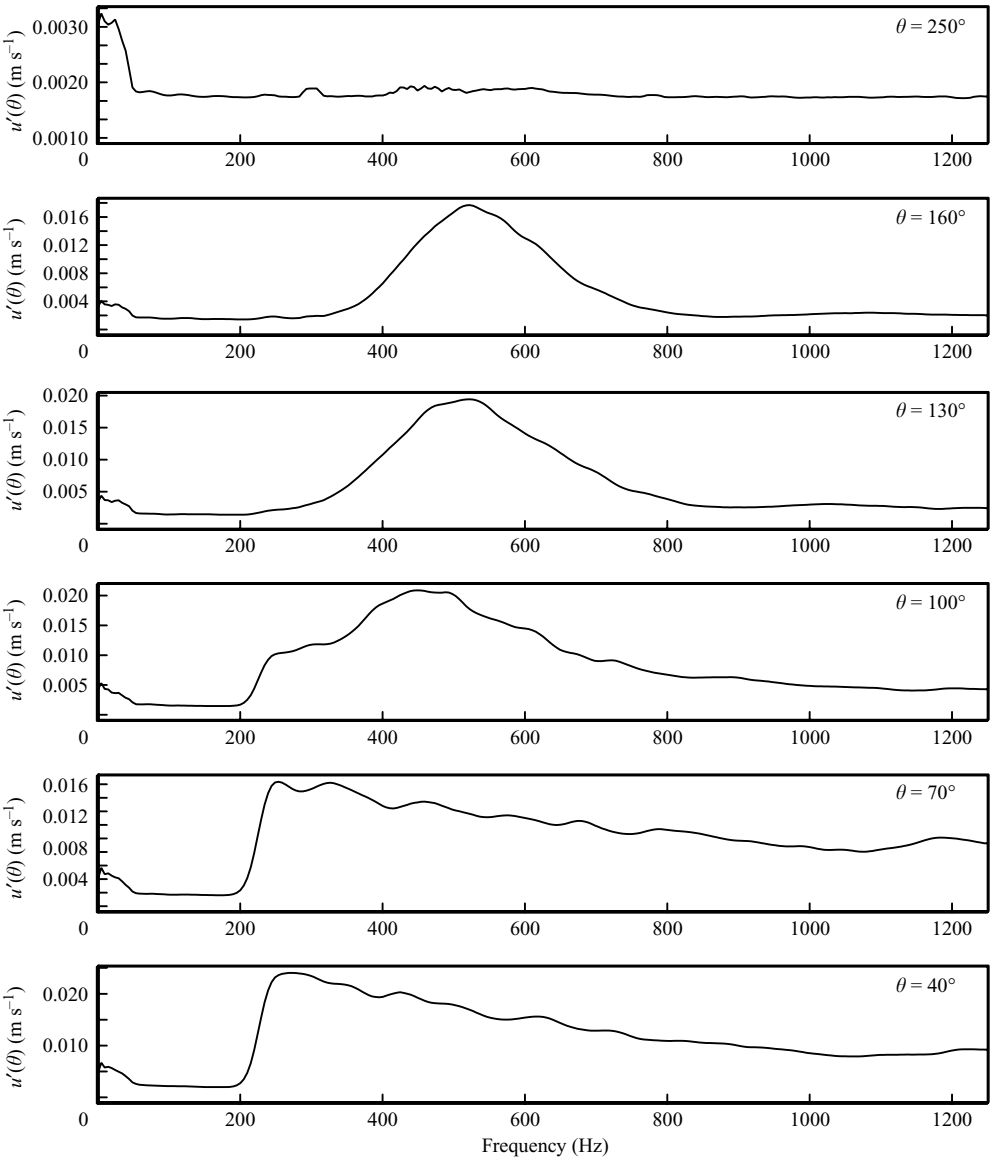


FIGURE 11. Spectra of maximum azimuthal velocity fluctuations at $Re = 437$ for different relative angles from the low amplitude (28 p.s.i.) pulse generator. $r/r_c = 1.53$.

background level. The background level was computed for each ensemble average in the range $3 \leqslant t/T \leqslant 4$.

The result of determining the wave packet leading and trailing edges for the lower amplitude (28 p.s.i.g.) air pulse is presented in figure 15. The squares mark all of the leading edges of the wave packets at every position. The triangles mark all of the trailing edges. The distances between the leading and trailing edge pairs represent individual wave packets. Singly they might appear as 'fingers' that are elongated in the R-direction and slightly inclined in the time-direction. A good example of this is shown in figure 15(a) of Lingwood (1996). As the wave packets develop radially, they merge together. Therefore, what is ultimately important is the upper bound in

https://doi.org/10.1017/S0022112006001546 Published online by Cambridge University Press

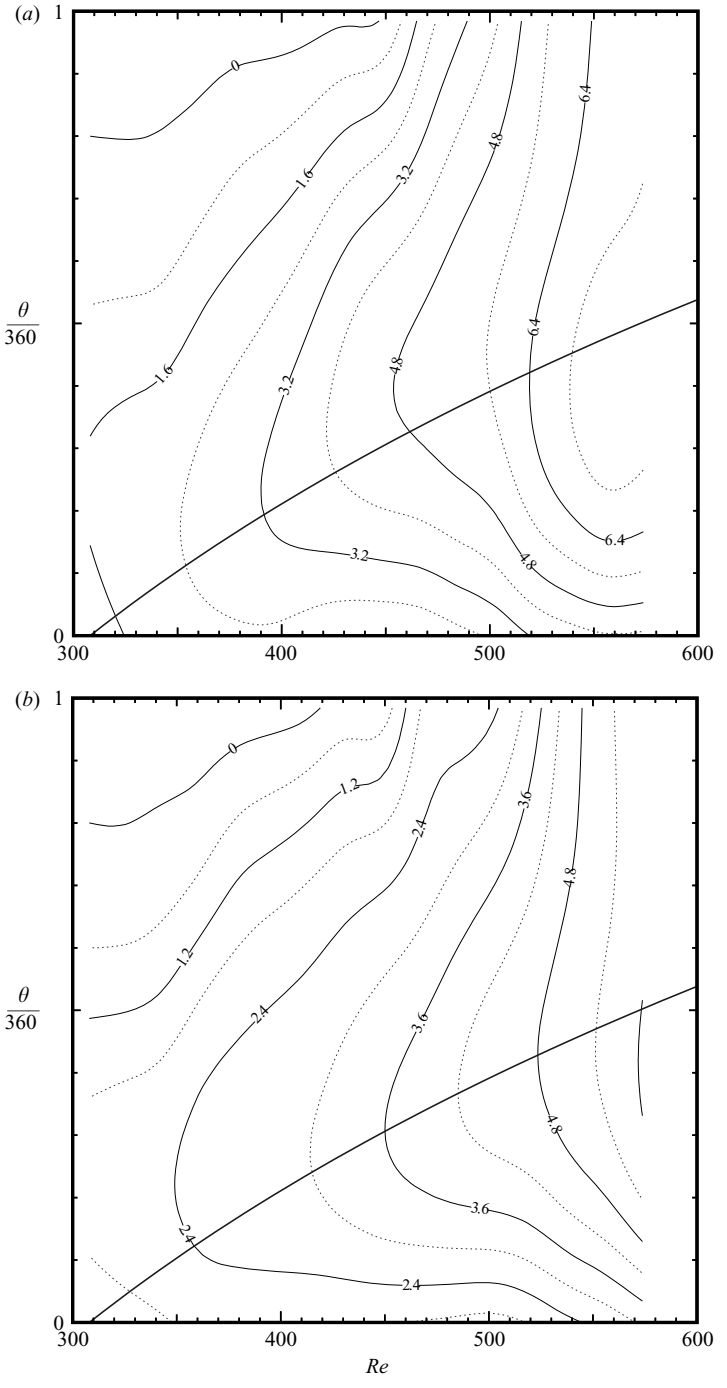


FIGURE 12. Spatial amplitude distributions produced by low pressure (28 p.s.i.) pulse generator, and shown as contours of $\log(u'(\theta)/u'(\theta)_{min})$ for frequencies of (*a*) 533 Hz and (*b*) 1000 Hz. The curve corresponds to log-spiral with a spiral angle of $\psi = 11.1^\circ$ that originates from disturbance source.

https://doi.org/10.1017/S0022112006001546 Published online by Cambridge University Press

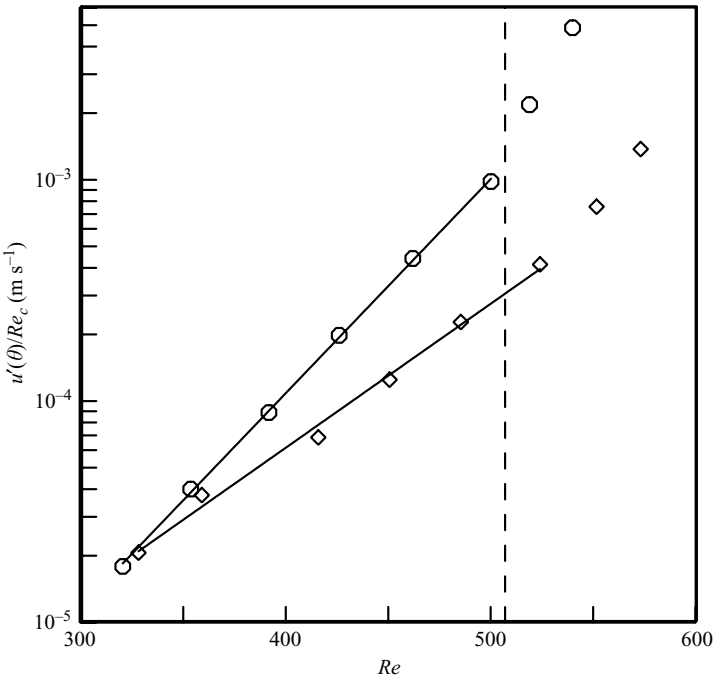


FIGURE 13. Spatial development of r.m.s. azimuthal velocity fluctuations measured along log-spiral in figure 12 for ○, 533 Hz ($-\alpha_i Re_c = 0.0223$) and ◇, 1000 Hz ($-\alpha_i/Re_c = 0.0150$) with low pressure (28 p.s.i.) pulse generator. Lines correspond to a least-squares curve fit of the data to an exponential function.

time of the trailing edges and the lower bound in time of the leading edges. For reference, the solid curves mark the bounds drawn by Lingwood (1996). The dotted curve corresponds to the space–time development of the trailing edge of a $n = 67$ disturbance for the linear simulation of Davies & Carpenter (2003). The vertical dashed line marks R_{c_A}.

With regard to our objectives, in making comparisons to Lingwood's (1996) experiment, the important comparison is with the development of the disturbance packet trailing edge, near R_{c_A}. We might expect some differences to occur close to the disturbance source because of the differences in approach and the need for some development length for disturbances to be amplified by the flow. However, in the range of Reynolds numbers between 400 to 475, the agreement is very good.

Above $R = 475$, Lingwood (1996) predicted an acceleration of the temporal spreading of the wave-packet trailing edge. This was largely extrapolated since the largest measurement Reynolds number was approximately 480.

In our case, we observe a deceleration of the trailing-edge temporal spreading to which it is asymptotically approaching a constant. The same behavior was predicted by Davies & Carpenter (2003). Their conclusion was that although the higher frequencies were absolutely unstable, this did not produce a global mode and they were still dominated by the convective instability.

The spatio-temporal development of the disturbance wave packets is further illustrated in figure 16 which shows contours of the peak amplitude of the wave packets. As in figure 12, the amplitudes have been normalized by the minimum value and displayed as log-scale contours to highlight linear growth. The heavier solid

https://doi.org/10.1017/S0022112006001546 Published online by Cambridge University Press

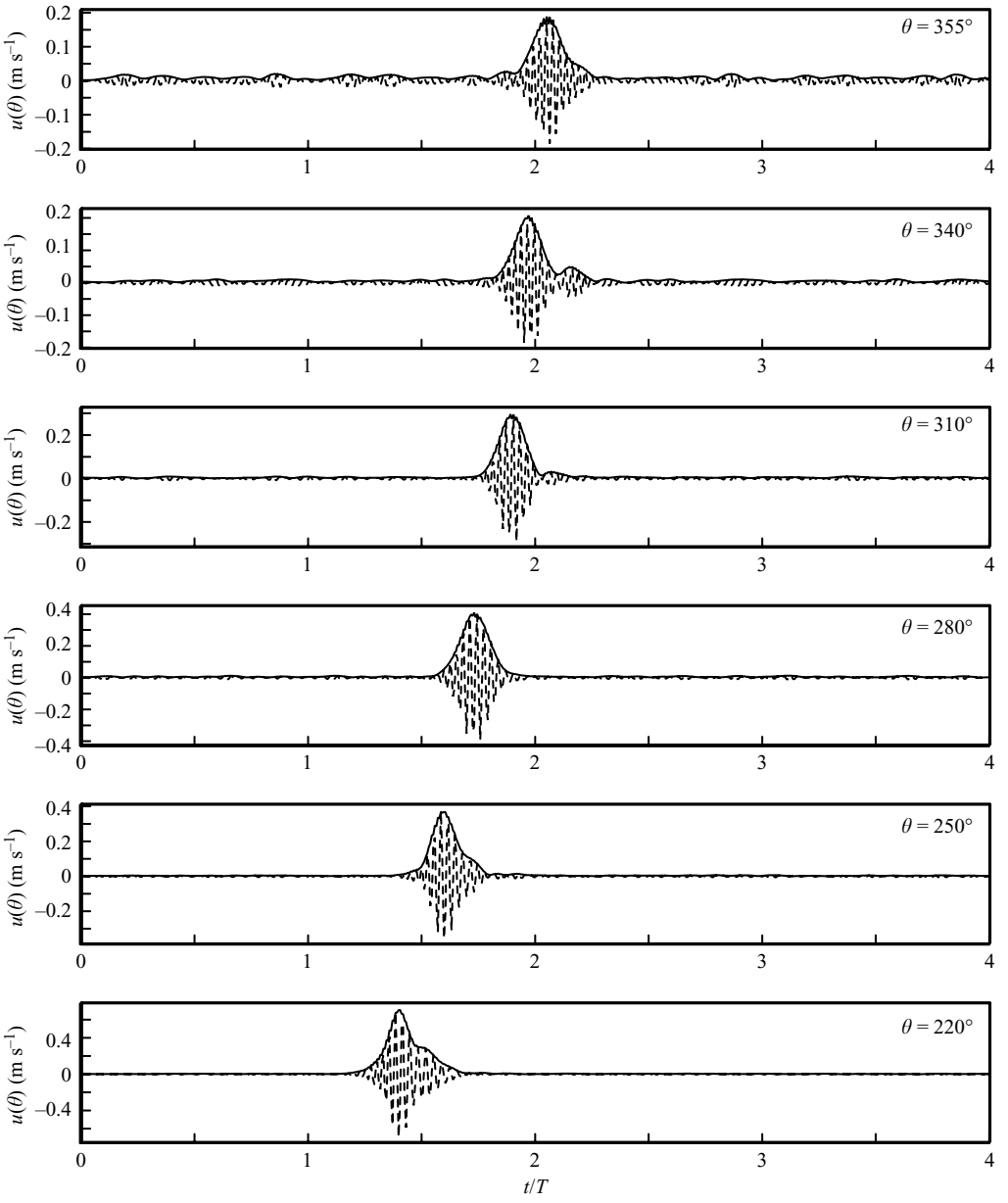


FIGURE 14. Ensemble-averaged azimuthal velocity time series measured at different azimuthal angles at $Re = 514$ for lower (28 p.s.i.) amplitude pulse. Dashed curve, ensemble-averaged velocity; solid curve, amplitude envelope produced by a digital Hilbert filter of our design.

lines represent propagation boundaries with spreading rates taken from the linear simulation of Davies & Carpenter (2003). These lines are found to encompass the disturbance amplitude evolution well. The development of the peak amplitude of the wave packets appears to be largely convective, with no abrupt changes in the vicinity of R_{c_A}. The maximum amplitude occurs at $R \simeq 530$ which is comparable to the natural development shown in figure 7.

https://doi.org/10.1017/S0022112006001546 Published online by Cambridge University Press

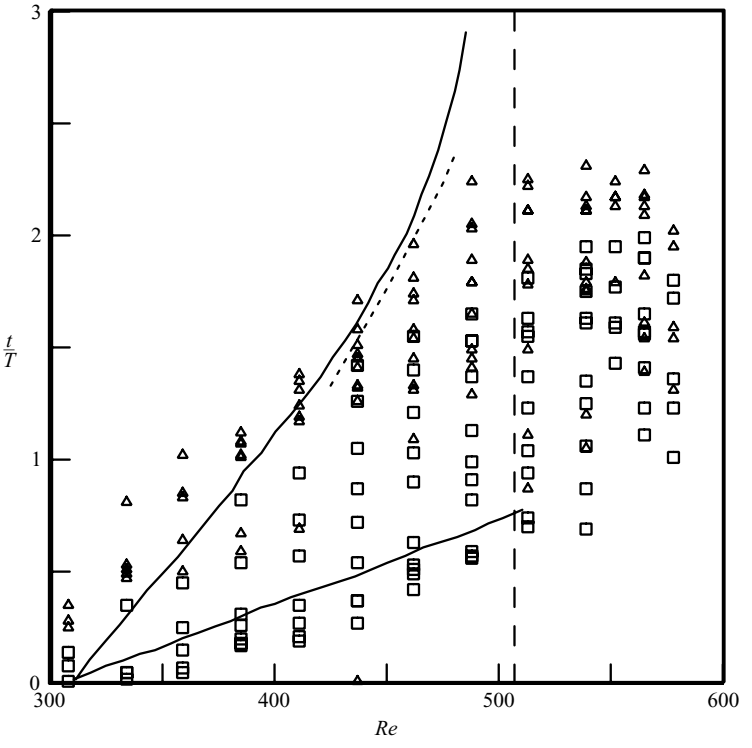


FIGURE 15. Space–time map of □, leading- and Δ, trailing-edge locations of disturbance wave packets for lower (28 p.s.i.) amplitude pulse. Solid curves are the trend from Lingwood (1996). The dashed line is from the linear simulation of Davies & Carpenter (2003).

3.2.2. *High-amplitude pulse*

The higher pressure (80 p.s.i.g) air pulse was intended to examine the effect of larger disturbance amplitudes on the development of the wave packets close to R_{c_A}. As with the lower amplitude pulse case, we examined the full spatial evolution of the disturbance in this case by compiling spectra at different (r, θ) locations. The result of this is presented in figures 17(a) and 17(b). These plots are comparable to those in figure 12 and focus on the same frequencies of 533 and 1000 Hz. The amplitudes have again been normalized by their minimum value and are presented as log-level contours to highlight exponential growth. The solid curve again corresponds to a log-spiral with a spiral angle of $\psi = 11.1^\circ$ that is based on $\beta = 0.0698$ and the most amplified $\alpha_r = 0.354$.

As before, amplitudes along the log-spiral were compiled and plotted. These are shown in figure 18. The symbols correspond to the $u'(\theta)$ values normalized by R_{c_I}. The solid lines correspond to the exponential fit for the respective frequencies at the lower pressure condition that was shown in figure 13.

For linear disturbances at higher initial amplitudes, we expect a shift in the amplitude, with the growth rate remaining the same. In this case, neither of the frequencies have such well-defined linear regions as the lower disturbance case (figure 13). For $f = 533$ Hz, if we include only the first five points, a good linear fit is obtained, but the amplification rate is larger than before. If we include all the points up to R_{c_A}, a linear fit yields approximately the same amplification rate as before, but the fit is

https://doi.org/10.1017/S0022112006001546 Published online by Cambridge University Press

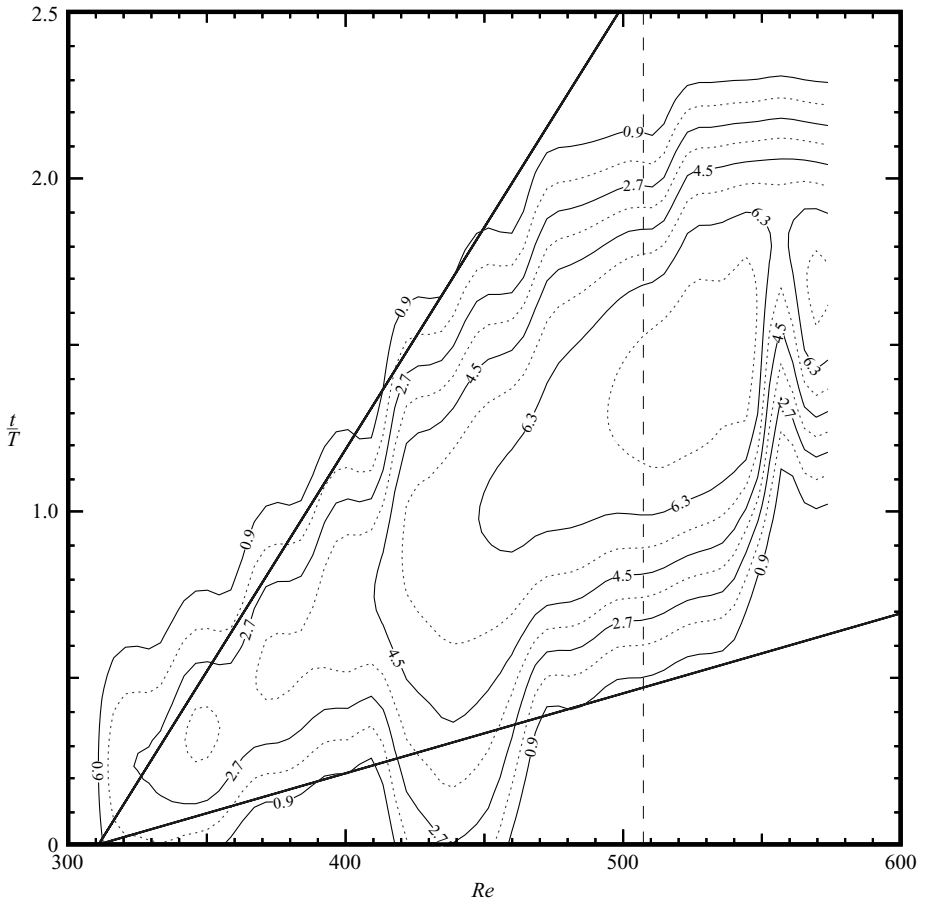


FIGURE 16. Space–time map of maximum wave packet envelope amplitude for lower (28 p.s.i.) amplitude pulse. Contours are $\log(u'(\theta)/u'(\theta)_{min})$. Solid lines are based on linear simulations of Davies & Carpenter (2003). The dashed line marks absolute instability critical Reynolds number. Note edge of disk is at $Re = 586.95$.

not nearly as good. For $f = 1000$ Hz, a linear fit of the first three or the last four points yields the same growth rate. Therefore, a fit that includes all the points gives approximately the same value as the lower disturbance case, although again the fit is not as good.

Overall we can conclude that the higher pulse amplitude increased the amplitude of the most amplified frequencies. There is also a possibility that its development was weakly nonlinear. The amplitude and growth rate of higher frequencies expected to be absolutely unstable did not appear to change with the higher disturbance pulse.

We next examined the effect of the higher-pressure pulse on the development of the wave packets. Ensemble-averaged time series that illustrate this at $R = 514$ are shown in figure 19. Note that this is the same Reynolds number as the ensemble-averaged time series shown in figure 14. Comparing the two cases, the higher-pressure pulse has produced a noticeable increase in the spreading of the trailing edge (right-hand side) of the wave packets. The leading edges (left-hand side) show virtually no change.

The locations of the leading and trailing edges of the wave packets in this case were analysed as before. The space–time development of the wave packet spreading

https://doi.org/10.1017/S0022112006001546 Published online by Cambridge University Press

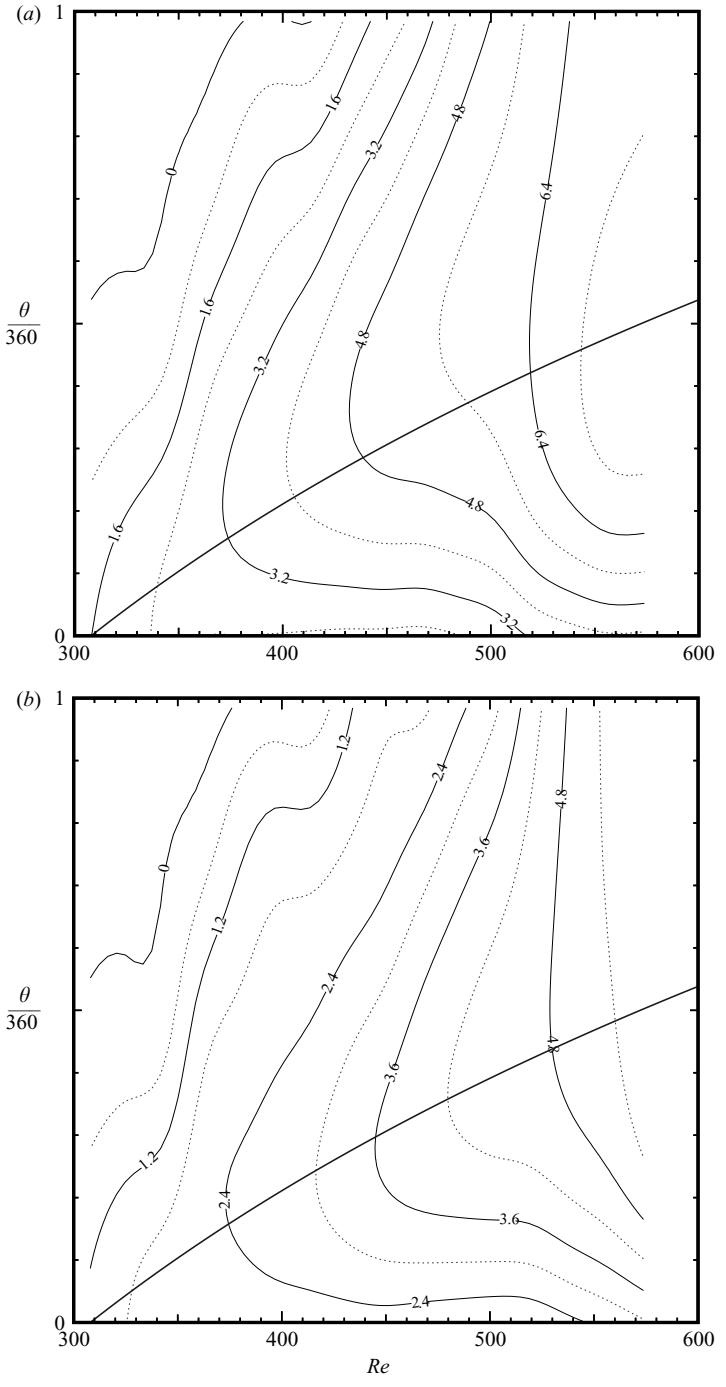


FIGURE 17. Spatial amplitude distributions produced by high-pressure (80 p.s.i.) pulse generator, and shown as contours of $\log(u'(\theta)/u'(\theta)_{min})$ for frequencies of (*a*) 533 Hz and (*b*) 1000 Hz. The curve corresponds to log-spiral with a spiral angle of $\psi = 11.1^\circ$ that originates from disturbance source.

https://doi.org/10.1017/S0022112006001546 Published online by Cambridge University Press

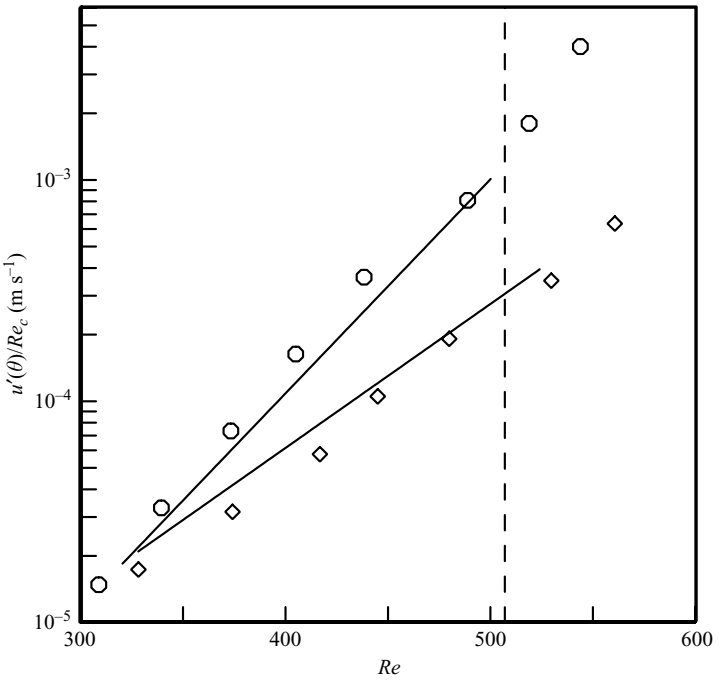


FIGURE 18. Spatial development of r.m.s. azimuthal velocity fluctuations measured along log-spiral in figure 17 for ○, 533 Hz ($-\alpha_i Re_c = 0.0223$) and ◇, 1000 Hz ($-\alpha_i Re_c = 0.0150$) with high-pressure (80 p.s.i.) pulse generator. Lines correspond to exponential fit from figure 13 for low-pressure pulse.

is summarized in figure 20. The corresponding result at the lower pulse pressure was shown in figure 15. As before, the squares mark all of the leading edges of the wave packets at every position, and the triangles mark all of the trailing edges. The distance between the leading- and trailing-edge pairs represent individual wave packets. Again for reference, the solid curves mark the bounds drawn by Lingwood (1996), and the vertical dashed line marks R_{c_A}.

Again, the important comparison we are making is with the development of the wave packet trailing edges near R_{c_A}. Closer to the disturbance source, the larger pulse levels have produced an overall initially faster expansion of the wave packets, both on the leading and trailing edges. These, however, developed relatively parallel to the solid curves representing Lingwood's (1996) trend.

Focusing on the trailing-edge development close to R_{c_A}, we do not observe the same type of deceleration of the temporal spreading observed with the lower-amplitude pulse. In the previous case, the trailing edge reached an asymptote at $t/T \simeq 2.3$. In the present case, by the last measurement position inboard of R_{c_A}, the trailing-edge location is approximately $t/T = 2.8$. More importantly, it has a trend that more closely follows Lingwood's (1996) expectation.

Beyond R_{c_A}, the leading and trailing edges of isolated wave packets became more difficult to specify in the ensemble averages at the large relative azimuthal angles. This resulted in a lack of points at larger t/T for $R > R_{c_A}$. Even with this difficulty, a significant number of t/T values of trailing edges that were larger than the largest for the lower pulse amplitude can be identified.

https://doi.org/10.1017/S0022112006001546 Published online by Cambridge University Press

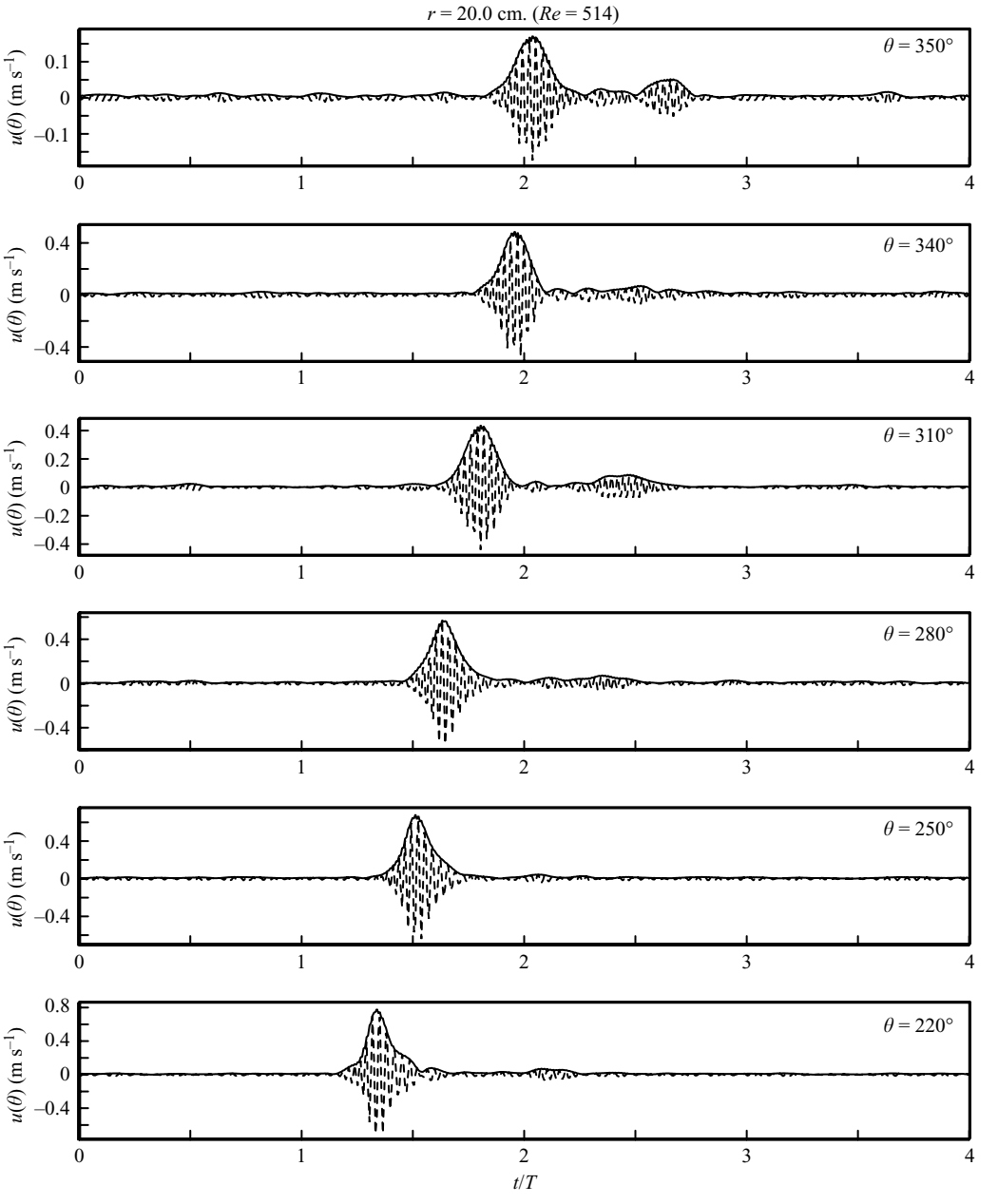


FIGURE 19. Ensemble-averaged azimuthal velocity time series measured at different azimuthal angles at $Re = 514$ for higher (80 p.s.i.) amplitude pulse. $r = 20$ cm. Dashed curve, ensemble-averaged velocity; solid curve, amplitude envelope produced by a digital Hilbert filter of our design.

The higher-pressure pulse was found to significantly change the character of the peak amplitude of the wave packets beyond R_{c_A}. This is shown in figure 21, which directly compares to figure 16 for the lower pulse amplitude. Here again, the the amplitudes have been normalized by the minimum value and displayed on a log-scale contours to highlight linear growth. The heavier solid lines again represent

https://doi.org/10.1017/S0022112006001546 Published online by Cambridge University Press

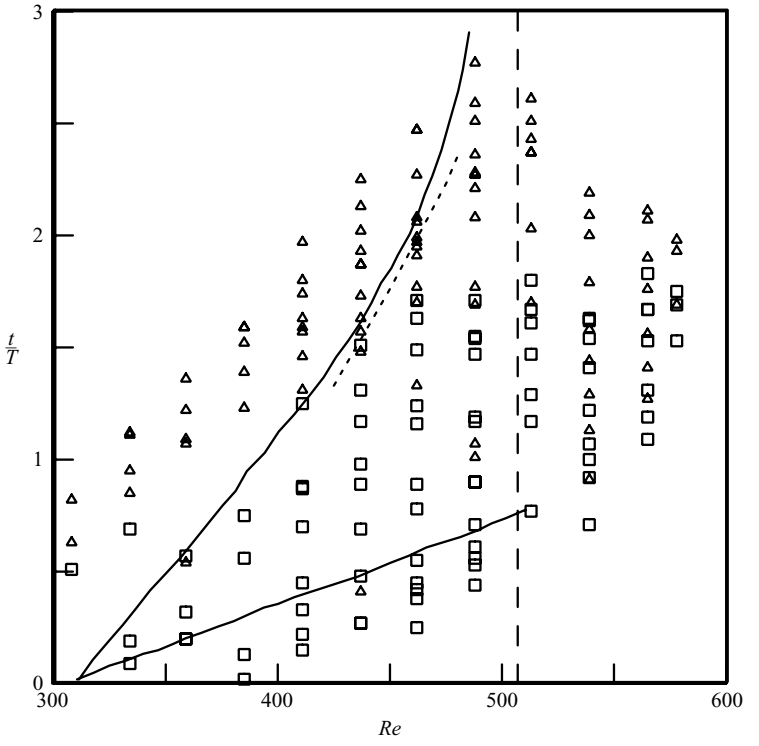


FIGURE 20. Space–time map of □, leading- and △, trailing-edge locations of disturbance wave packets for higher (80 p.s.i.) amplitude pulse. Solid curves are trend from Lingwood (1996). Dashed line is from linear simulation of Davies & Carpenter (2003).

propagation boundaries with spreading rates taken from the linear simulation of Davies & Carpenter (2003). The vertical dashed line denotes R_{c_A}.

Aside from some additional initial temporal spreading of the wave packet amplitude, the development for $R < R_{c_A}$ is comparable to that with the lower pulse amplitude. However, just beyond the critical Reynolds number, there was a rapid temporal growth in amplitude of the wave packet that was not observed at the lower pulse amplitude.

4. Discussion of results

The principal objective of this work was to reconcile inconsistencies in the temporal growth of disturbance wave packets near R_{c_A} between Lingwood's (1996) experiment, and the linear simulations of Davies & Carpenter (2003), as well as to understand the role the absolute instability has on transition to turbulence of boundary layers on a rotating disk. To accomplish this, we paid particular attention to minimizing background disturbances, especially those resulting from surface imperfections to which the crossflow instability is exceedingly sensitive. In this regard, we developed a method for introducing controlled temporal disturbances from outside the boundary layer. This had the advantage of not placing a hole through the disk surface such as was done by Lingwood (1996), and that was known (Wilkinson *et al.* 1989) to produce a stationary disturbance wedge around the disk. The motivation for these

https://doi.org/10.1017/S0022112006001546 Published online by Cambridge University Press

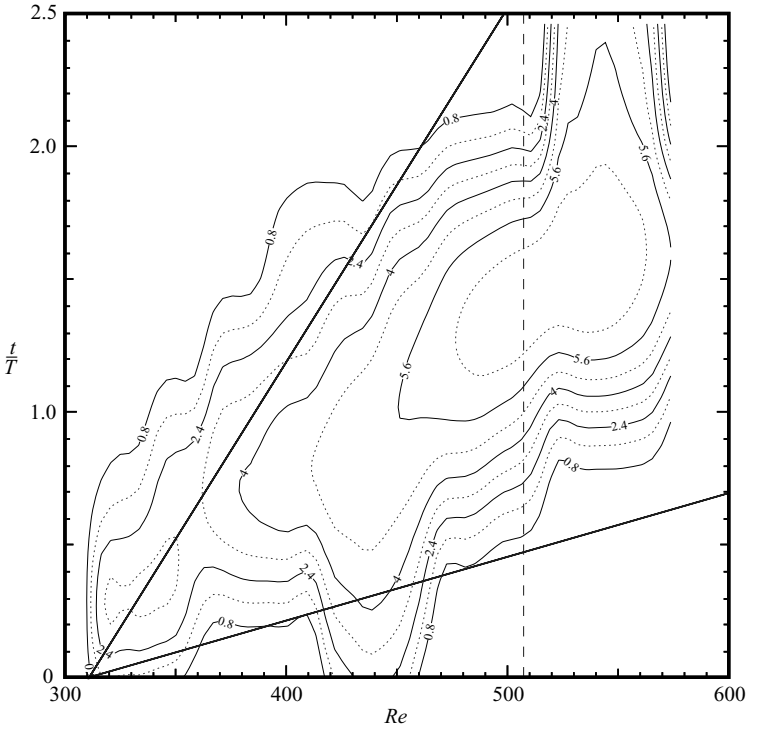


FIGURE 21. Space–time map of maximum wave packet envelope amplitude for higher (80 p.s.i.) amplitude pulse. Contours are $\log(u'(\theta)/u'(\theta)_{min})$. Solid lines are based on linear simulations of Davies & Carpenter (2003). Dashed line marks absolute instability critical Reynolds number. Note edge of disk is at $Re = 586.95$.

steps was twofold: (i) to limit the amplitude of stationary modes and thereby provide the potential for following travelling disturbance wave packets closer to R_{c_A}, and (ii) to lower background disturbance levels so that controlled disturbances above the background level, could be minimized to assure that they be linear in accordance with the assumptions of Lingwood's (1995) analysis and Davies & Carpenter's (2003) simulation.

A secondary objective of this work was to examine the effect of larger disturbance amplitudes on the development of the wave packets close to R_{c_A}. This led to a second experimental condition.

The quality of the experimental set-up was indicated by documenting the basic flow and its linear stability characteristics. The mean flow was found to agree well with the analytic profile for an infinite radius disk. The only deviation came at the largest radii. We associated this with mean flow distortion brought on by the transition to turbulence. The location of the mean flow distortion coincided with that of the amplitude saturation at the end of the linear growth region of the band of most amplified frequencies. Based on both of these characteristics, we judged transition to turbulence to occur at $R \simeq 539$. This agreed well with previous measurements in the same facility by Knasiak (1996), and measurements in a different rotating disk facility by Wilkinson & Malik (1985). Both of these had been with low disturbance 'clean' disks, and with measurements based on hot-wire sensors. The present measurements placed R_{TR} about 6 % larger than R_{c_A}. This provided the first indication that the

https://doi.org/10.1017/S0022112006001546 Published online by Cambridge University Press

absolute instability was not the dominating mechanism for transition to turbulence at the low disturbance levels present in our experiment.

A more sensitive quantification of the basic flow came by documenting its stability characteristics. Spectral analysis of $u(\theta)$ velocity fluctuations revealed growth in a frequency band that agreed with the most amplified Type I crossflow modes predicted from linear theory. The wall-normal amplitude distributions were found to agree well with the linear theory eigenfunction. In addition, the radial development of maximum amplitude of the most amplified frequencies exhibited clear linear (exponential) growth regions. The amplification rates were very close to those found by Corke & Knasiak (1998) who used wall 'dots' to enhance specific azimuthal mode numbers. In addition, an average value of the amplification rates of the most amplified frequencies was within 8 % of that predicted for a pure wave by Mack (1985), and within 2 % of the value predicted from DNS simulations by Spalart (1991) for random stationary disturbances.

When introducing the controlled temporal disturbances, we selected two initial amplitudes (designated by the source pressure settings used). The velocity spectra revealed that both pulse amplitude conditions put energy into a range of frequencies that was capable of being amplified by the Type I crossflow modes ($f \geqslant 300$ Hz), and to be a part of the absolute instability ($f \geqslant 833$ Hz). The higher pulse amplitude produced higher initial fluctuation levels, with about the same frequency distribution as the lower-amplitude pulse.

Two frequencies, one representing the most amplified linear range (533 Hz) and the other representing the absolute instability range (1000 Hz) were analysed in detail to verify their amplitudes and growth rates for the two temporal disturbances cases. This was done by measuring their amplitudes from spectra of the wave packets. The growth in amplitude was determined by following a log-spiral (r, θ) trajectory with a 11.1° spiral angle that corresponded to the most amplified wavenumbers.

For the low-pressure pulse, both frequencies exhibited clear linear growth starting from the disturbance origin out to R_{c_A}. This was an important result that substantiated our objective that the lower-amplitude temporal disturbances be linear.

The higher-pressure pulse was found to increase the amplitude of the most amplified (533 Hz) frequencies. In addition, based on a comparison with the lower pressure pulse case, there was a possibility that the development of the most amplified frequency was weakly nonlinear. In contrast, the amplitude and growth rate of the higher frequencies in the absolutely unstable band with the higher pressure pulse, appeared to be unchanged compared with the lower-pressure pulse.

The controlled temporal disturbances at the two pressures were each found to lead to identifiable wave packets. The edges of the wave packets were determined from an amplitude envelope that was found using a digital Hilbert filter of our design. The method involved locating the peak in the envelope amplitude, then moving forward and backwards in time to find the point where the amplitude envelope reached the background level. The background level was computed in a large time region that was out of the range of the wave packets.

The spreading of the disturbance wave packet leading and trailing edges was used by Lingwood (1996) as evidence of the absolute instability. In making comparisons to Lingwood's experiment, the important comparison is with the development of the disturbance packet trailing edge, near $R_{c_A} = 507$.

For the lower-amplitude (lower-pressure) disturbances, we initially observed some differences from Lingwood in the temporal extent of the wave packet trailing edge at small radii, close to the source. This may have been due to the different approach

https://doi.org/10.1017/S0022112006001546 Published online by Cambridge University Press

used in producing the disturbances. However, after a short development distance, fairly good agreement was found in the range of Reynolds numbers from 400 to 475.

In the experiment, Lingwood (1996) had extrapolated an acceleration of the temporal spreading of the wave packet trailing edge based on results up to the largest measurement Reynolds number of 480. In our case, we observed a deceleration of the trailing-edge temporal spreading which is asymptotically approaching a constant. The same behaviour was observed by Davies & Carpenter (2003) in their linear simulations. Their conclusion was that although the higher frequencies were absolutely unstable, this did not produce a global mode, and they were still dominated by the convective instability.

This was further reinforced by following the space–time development of the peak amplitude of the wave packets for the lower initial disturbance condition. These showed a linear spreading of the wave packet amplitude in time and space from the disturbance source. There were no abrupt changes in the wave packet amplitude near R_{c_A}. The maximum amplitude occurred at approximately $R = 530$, close to the transition Reynolds number we had observed for the low disturbance basic flow (539).

With the higher-amplitude (higher-pressure) disturbances, there was no effect on the space–time development of the wave packet leading edges. However, there was a noticeable increase in the temporal extent of the trailing edges. The increase in the temporal extent of the trailing edges was evident all the way back to the disturbance source location. Aside from the more extended trailing edges, the space–time development was comparable to that denoted by Lingwood (1996). In this case as R_{c_A} was approached, the temporal extent (t/T) of the wave packets was approximately 22 % larger than in the previous low-amplitude case. Just beyond R_{c_A}, the temporal extent of the trailing edge of wave packets was still 13 % larger than wave packets with the lower initial disturbance. Although the trend agrees better with Lingwoods's experiment, it is not conclusive that the rate of temporal spreading of the wave packet trailing edges was increasing.

The space–time development of the peak amplitude of the wave packets for this higher initial disturbance condition offers a different perspective. With the lower initial disturbance condition, there were no distinguishing features in the wave packet amplitude near R_{c_A}. In contrast to that, with the higher initial disturbance amplitude, we observed an abrupt increase in the wave packet amplitude at large times where we expect the accelerated spreading of the trailing edge.

Is this evidence of the absolute instability? Or possibly is this rapid growth in amplitude brought on by higher amplitudes that triggered the global mode predicted by Pier (2003)? The spectra that was used to document the spatial development of energy in the band of absolutely unstable frequencies with 1000 Hz being an example, indicated a linear (exponential) growth in that band. The amplitude of the higher-frequency band was approximately 40 % as large as the most amplified frequency (533 Hz) at Re_{c_A}, so that it was not insignificant.

What triggered the difference in the growth in amplitude of the wave packets past Re_{c_A} with the larger pulse amplitude? The amplitude of the most amplified frequency was larger with the larger pulse amplitude. In addition, depending on how you fit the spatial growth, the amplification rate increased over that with the lower-amplitude pulse, which is not possible according to linear theory. Therefore, we might conclude that the higher-amplitude pulse produced a weak nonlinearity at the most amplified frequencies. These frequencies are, however, not those that are predicted to be absolutely unstable. In fact, those frequencies appeared to be unchanged in terms of amplitude and amplification rate with the higher pulse amplitude. Thus, it does not appear that the energy in the higher absolutely unstable frequencies has reached

https://doi.org/10.1017/S0022112006001546 Published online by Cambridge University Press

nonlinear levels near Re_{c_A}, which is a prerequisite for the secondary absolute instability scenario of Pier (2003). Therefore, although we can substantiate the results of the linear simulation of Davies & Carpenter (2003), which was our primary objective, we do not have sufficient evidence to address the question of whether the higher amplitude condition triggered a global mode.

5. Conclusions

The experiment was designed to study the role of the absolute instability on transition to turbulence of the flow over a rotating disk. This was in light of inconsistent observations in the present experiment and by others, of transition Reynolds numbers for low-disturbance ('clean' disk) conditions that exceeded R_{c_A} by 6–8 %. In addition, the linear numerical simulation by Davies & Carpenter (2003) indicates that the absolute instability of the disk flow is not sustained for long times and that convective behavior dominates.

The experiment verified a new approach for introducing temporal disturbances through air pulses that were introduced above the disk, outside the boundary layer. This eliminated any stationary disturbances that might come by placing the disturbance generator on the disk surface. Two pulse amplitudes were used. The lower amplitude was verified to produce disturbance wave packets that had linear characteristics. This was important to allow a direct comparison to the linear simulations.

The disturbance wave packets that were produced by the low-amplitude pulse agreed well with the space–time development found in Lingwood's (1996) experiment up to approximately 95 % of R_{c_A}. However, rather than an acceleration of the trailing-edge spreading of the wave packet that had been extrapolated by Lingwood as R_{c_A} was further approached, we observed a deceleration of the trailing-edge spreading towards an asymptote past R_{c_A}. This result agrees with the observations of Davies & Carpenter (2003). The space–time development of the maximum of the wave packet amplitude envelope showed a linear spreading with no abrupt changes in amplitude near R_{c_A}. The maximum amplitude occurred at approximately $R = 530$, which was past R_{c_A}, and close to the transition Reynolds number that been had observed for the basic flow (539).

The higher initial disturbance amplitude produced larger temporal spreading of the wave packets all the way down to the source location. Otherwise, the space–time development was similar to the case with the lower initial amplitude. However within 5 % of R_{c_A}, the temporal extent of the wave packets continued to grow, and was approximately 22 % larger than in the previous low-amplitude case. Although the trend agreed better with Lingwood's experiment, it is not conclusive that the rate of temporal spreading of the wave packet trailing edges was increasing. However, an abrupt increase in the maximum amplitude of the wave packet was observed just beyond R_{c_A} that was not present at the lower initial amplitude. This suggests that the amplitude development was not purely convective. In this case, the initial amplitude development of the most amplified frequencies appeared weakly nonlinear. However, the higher frequencies that are expected to be absolutely unstable continued to show linear characteristics with the higher initial amplitude. Therefore, they do not to appear satisfy the conditions of Pier (2003) that are required to excite a global instability in this case.

The authors are grateful to NASA Langley Research Center and Mr Steven Wilkinson for providing the motorized air bearing spindle that was used in the experiment. H. O. was supported by the Ministry of Higher Education in Egypt.

https://doi.org/10.1017/S0022112006001546 Published online by Cambridge University Press

REFERENCES

Corke, T. C. & Knasiak, K. F. 1994 Cross-flow instability with periodic distributed roughness. *Transition, Turbulence, and Combustion*, vol. 1, pp. 43–62, Kluwer.

Corke, T. C. & Knasiak, K. F. 1998 Stationary Travelling cross-flow mode interactions on a rotating disk. *J. Fluid Mech.* **355**, 285–315.

Corke, T. C. & Matlis, E. H. 2004 Transition to turbulence in 3-D boundary layers on a rotating disk – triad resonance. *IUTAM Symposium on 100 Years Boundary Layer Research* (ed. G. E. A. Meier & K. R. Sreenivasan). Kluwer.

Davies, C. & Carpenter, P. W. 2003 Global behaviour corresponding to the absolute instability of the rotating-disc boundary layer. *J. Fluid Mech.* **486**, 287–329.

Faller, A. J. 1991. Instability and transition of disturbance flow over a rotating disk. *J. Fluid Mech.* **230**, 245–269.

Fedorov, B. I., Plavink, G. Z., Prokhorov, I. V. & Zhuknoviskii, L. G. 1976 Transitional flow conditions on a rotating disk. *J. Engng Phys.* **31**, 1448–1453.

Gregory, N., Stuart, J. T. & Walker, W. S. 1955 On the stability of three-dimensional boundary layers with application to the flow due to a rotating disk. *Phil. Trans. R. Soc. Lond.* A **248**, 155–199.

Knasiak, K. 1996 Stability of rotating disk flow with distributed roughness: linear and nonlinear development. MS thesis, Illinois Institute of Technology, Chicago.

Kobayashi, R., Kohama, Y. & Takamadate, Ch. 1980 Spiral vortices in boundary layer transition regime on a rotating disk. *Acta Mech.* **35**, 71–82.

Lingwood, R. J. 1995 Absolute instability of the boundary layer on a rotating disk. *J. Fluid Mech.* **299**, 17–33.

Lingwood, R. J. 1996 An experimental study of absolute instability of the rotating-disk boundary-layer flow. *J. Fluid Mech.* **314**, 373–405.

Lingwood, R. J. 1997 On the effect of suction and injection on the absolute instability of the rotating-disk boundary layer. *Phys. Fluids* **9**, 1317–1328.

Mack, L. M. 1985 The wave pattern produced by a point source on a rotating disk. *AIAA Paper* 85-0490.

Malik, M. R., Wilkinson, S. P. & Orszag, S. A. 1981 Instability and transition in rotating disk flow. *AIAA J.* **19**, 1131–1138.

Othman, H. 2005 Experimental study of absolute instability over a rotating disk. PhD thesis, University of Notre Dame, Aerospace and Mechanical Engineering Department, Notre Dame, IN, USA.

Pier, B. 2003 Finite-amplitude crossflow vortices, secondary instability and transistion in the rotating-disk boundary layer. *J. Fluid Mech.* **487**, 315–343.

Saric, W. S., Reed, H. L. & White, E. B. 2003 Stability and transition of three-dimensional boundary layers. *Annu. Rev. Fluid Mech.* **35**, 413–440.

Smith, N. H. 1946 Exploratory investigation of laminar boundary layer oscillations on a rotating disk. *NACA* TN-1227.

Spalart, P. S. 1991 On the crossflow instability near a rotating disk. *Proc. R. A. S. Boundary Layer Transition and Control, Paper No.* 22.1, *Cambridge, U.K.*

Wilkinson, S. P. & Malik, M. R. 1985 Stability experiments in the flow over a rotating disk. *AIAA J.* **23**, 588–595.

Wilkinson, S., Blachard, A., Gaster, M., Tritz, T., Gad-el-Hak, M. & Selby, G. 1989 Flow visualization of a wave packet on a rotating disk. *Instability and transition*, p. 306. Springer.

https://doi.org/10.1017/S0022112006001546 Published online by Cambridge University Press